Type I interferon and MAVS signaling restricts chikungunya virus heart infection and cardiac tissue damage

Maria G. Noval[1,8], Eric Bartnicki[1], Sophie N. Spector[1], Franco Izzo[2,3], Payal Damani-Yokota[1], Navneet Narula[4], Stephen T. Yeung[1], Bruno A. Rodriguez-Rodriguez[1], M. Zahidunnabi Dewan[4], Valeria Mezzano[4], Cynthia Loomis[4,5], Kamal M. Khanna[1,6], and Kenneth A. Stapleford[1,7,8]

[1]Department of Microbiology, New York University Grossman School of Medicine, New York, NY, USA
[2]New York Genome Center, New York, NY, USA
[3]Division of Hematology and Medical Oncology, Department of Medicine and Meyer Cancer Center, Weill Cornell Medicine, New York, NY, USA
[4]Department of Pathology, New York University Grossman School of Medicine, New York, NY, USA
[5]Division of Advanced Research Technologies, New York University Grossman School of Medicine, New York, NY, USA
[6]Perlmutter Cancer Center, New York University Grossman School of Medicine, New York, NY, USA
[7]Lead contact: Kenneth A. Stapleford. kenneth.stapleford@nyulangone.org
[8]Corresponding authors: Kenneth A. Stapleford. kenneth.stapleford@nyulangone.org and Maria G. Noval. maria.noval@nyulangone.org

SUMMARY

Chikungunya virus (CHIKV) infection has been associated with severe cardiac manifestations. However, how CHIKV infection leads to heart disease remains unknown. Using C57BL/6 mice, we show that cardiac fibroblasts are the main target of CHIKV infection in the heart, and that cardiac tissue infection induces a local and robust type I interferon (IFN-I) response in both infected and non-infected cardiac cells. The loss of IFN-I signaling results in increased CHIKV infection, virus spreading, and apoptosis in cardiac tissue. Importantly, signaling through the mitochondrial antiviral-signaling protein (MAVS) is essential for efficient CHIKV clearance from the heart. Indeed, persistent infection in cardiac tissue of MAVS-deficient mice leads to cardiac damage characterized by focal myocarditis and major vessel vasculitis. This study provides a new mouse model of CHIKV cardiac infection and mechanistic insight on how CHIKV can lead to cardiac damage, underscoring the importance of monitoring cardiac function in patients with CHIKV infections.

Key words: Chikungunya virus, atypical manifestations, heart, myocarditis, type-I interferon, MAVS.

INTRODUCTION

Arthropod-borne viruses (arboviruses) such as Zika virus, dengue virus, and chikungunya virus (CHIKV) are associated with the development of cardiomyopathies in patients (Alvarez et al., 2017; Araiza-Garaygordobil et al., 2021; Minhas et al., 2017; Scatularo et al., 2022; Traverse et al., 2021). CHIKV-associated cardiac manifestations have been reported in more than 15 countries worldwide (Cotella et al., 2021; Traverse et al., 2021). These complications occur mainly within the first week after symptoms onset (Traverse et al., 2021), and include symptoms ranging from arrhythmias, atrial fibrillation, abnormal echocardiograms and electrocardiograms (Villamil-Gomez et al., 2016), reduction of the ejection fraction (Farias et al., 2019), myocarditis (Crosby et al., 2016; de Lima et al., 2021; Villamil-Gomez et al., 2016), to heart failure, and death (de Lima et al., 2021; Farias et al., 2019; Samra et al., 2017; Sharp et al., 2021). Indeed, more than 20% of the CHIKV-related mortality cases have been associated with cardiac complications (de Lima et al., 2021; Economopoulou et al., 2009; Sharp et al., 2021). Heart autopsies of individuals that succumbed to CHIKV infection reveal the presence of CHIKV antigen in the cardiac tissue (Lemant et al., 2008; Sharp et al., 2021), show immune cell infiltration indicative of viral myocarditis as well as signs of cardiac edema, endocarditis, necrosis, and cardiac congestion (de Lima et al., 2021). Although most of these complications are mainly observed in older adults and individuals with comorbidities (Hsu et al., 2019; Samra et al., 2017), cardiac manifestations associated with CHIKV infections have been reported in young individuals, including children and infants with no known comorbidities (de Lima et al., 2021; Farias et al., 2019; Villamil-Gomez et al., 2016). Despite the association of CHIKV with cardiac complications, whether cardiac tissue is a direct target of CHIKV infection, how the heart responds to CHIKV infection, and most importantly how CHIKV infection can lead to heart disease, remains largely unknown.

With global climate change and the emergence of arboviruses on the rise, there is an urgent need to address the understudied aspects of arboviral pathogenesis to develop intervention strategies for future outbreaks. Here, using a mouse model of CHIKV infection we demonstrate that CHIKV disseminates to the heart and infects cardiac tissue. We found that this infection is in part mediated by the presence of the CHIKV receptor MXRA8, and that the primary target of CHIKV infection are vimentin^{+}/αSMA^{-} cardiac fibroblasts. Moreover, we show that CHIKV infection results in active replication and generation of infectious particles within the cardiac tissue, and the heart infection is rapidly cleared without signs of tissue inflammation or cardiac tissue damage in wild type (WT) mice. We show that cardiac tissue infection induces activation of the type I IFN pathway (IFN-I) in both infected and non-infected cardiac cells, and the loss of IFN-I signaling results in increased CHIKV infection, virus spreading, and apoptosis in cardiac tissue. In addition, we found that signaling through the mitochondrial antiviral-signaling protein (MAVS), a central hub for signal transduction initiated by cytosolic

pattern recognition receptors (PRRs) RIG-I or MDA5, is essential for efficient CHIKV clearance, with viral particles being detected up to 10 days post infection (dpi) in *Mavs*$^{-/-}$ mice. Importantly, we found that persistence of CHIKV infection in cardiac tissue leads to cardiac tissue damage characterized by CD3^{+} and CD11b^{+} infiltrates in ventricles and atrium of *Mavs*$^{-/-}$ mice at 15 dpi characteristic of focal myocarditis and aorta (Ao) and pulmonary artery (PA) vasculitis that remains detectable up to 30 dpi. Overall, our results show that CHIKV directly infects cardiac tissue and demonstrate that a robust IFN-I response and MAVS signaling are essential to control CHIKV infection in the heart and prevent cardiac tissue damage.

RESULTS

Cardiac tissue is infected by CHIKV in a MXRA8-dependent manner. To explore cardiac tissue susceptibility to CHIKV infection, we used 6-week-old C57BL/6 mice as a model (Noval et al., 2019). We infected mice either intradermally through footpad injection, via natural transmission by mosquito bite, or intravenously via tail vein injection to bypass the requirement of initial dissemination from a primary infection site. We harvested mice at two or three days post-infection (dpi) depending on the inoculation route, perfused hearts to clear the tissue from residual blood and associated virus, and quantified CHIKV RNA by RT-qPCR and infectious virus by median tissue culture infectious dose ($TCID_{50}$). We were able to detect CHIKV genomes and infectious particles from perfused hearts in infected mice regardless of the inoculation route **(Figure 1A)**. To confirm the presence of actively replicating virus in the heart, we measured the ratio between CHIKV genomic and sub-genomic RNA at either 2 or 5 dpi after intravenous infection by RNA-seq. As a non-replicative control, we infected mice with heat-inactivated (HI) CHIKV. We detected higher amounts of reads mapping to CHIKV sub-genomic RNA in comparison to the full-length genomic RNA **(Figure 1B)** indicating active replicating viral RNA in cardiac tissue at both 2 and 5 dpi. The ratio of sub-genomic to genomic RNA at 2 dpi was higher than at 5 dpi (R = 5.6 vs. R = 2.2, respectively), suggesting that CHIKV is rapidly cleared from the infected tissue. These results demonstrate that CHIKV can both directly infect the heart as well as disseminate from the primary infection site to the cardiac tissue.

The MXRA8 protein is a well-established receptor mediating CHIKV infection in mammals (Zhang et al., 2019; Zhang et al., 2018). Therefore, we asked whether MXRA8 is required for CHIKV cardiac tissue infection. Using a *Mxra8* deficient mouse model (*Mxra8*$^{D8/D8}$), we observed that the absence of functional MXRA8 results in a significant reduction of CHIKV RNA in cardiac tissue following intradermal inoculation **(Figure 1C)**. This reduction in CHIKV RNA correlated with a decrease in the induction of *Isg15*, an interferon-stimulated gene (ISG) highly induced during CHIKV infection (Werneke et al., 2011), supporting reduced cardiac infection in MXRA8 deficient mice. Importantly, viral RNA levels in serum remained unaltered **(Figure 1C)**, excluding the possibility that the observed decrease in CHIKV infection in *Mxra8*$^{\Delta 8/\Delta 8}$ infected hearts is driven by reduced viremia. In addition, we infected *Mxra8*$^{\Delta 8/\Delta 8}$ and WT mice intravenously with a reporter CHIKV that expresses the ZsGreen fluorescent protein (CHIKV-ZsGreen) only under active viral replication (Noval et al., 2019) **(Figure S1A)** and found reduced CHIKV infection in *Mxra8*$^{\Delta 8/\Delta 8}$ cardiac tissue **(Figure 1D).** Notably, viral RNA levels in serum in *Mxra8*$^{\Delta 8/\Delta 8}$ mice inoculated intravenously are significantly reduced **(Figure 1D)**, suggesting distinct mechanisms regulating viremia in *Mxra8*$^{\Delta 8/\Delta 8}$ mice**.** Altogether, these data demonstrate that CHIKV can efficiently disseminate and infect cardiac tissue and that this infection is in part dependent on functional MXRA8.

Cardiac fibroblasts are the primary cellular target of CHIKV infection in infected hearts. We next sought to determine the CHIKV infection patterns and cellular targets within the cardiac tissue. Mice were infected with CHIKV-ZsGreen and cardiac tissue was harvested at 2 dpi. To address direct infection of cardiac tissue and to bypass the variability associated with differences in dissemination, we used the intravenous infection route unless stated otherwise. At 2 dpi, we prepared frozen heart sections and performed DAPI staining followed by confocal microscopy imaging **(Figure 2A, upper panel)**. We observed positive CHIKV-ZsGreen-infected cells forming discrete infection foci within the right ventricle (RV), left ventricle (LV), and septum **(Figure 2A, bottom panel)**, as well as in valves, perivascular region, and atrium **(Figure S1B-D).**

Since we found that MXRA8 is required for an efficient heart infection **(Figure 1C-D)**, we interrogated cell type-specific expression levels of the *Mxra8* receptor in cardiac tissue by leveraging the single-cell dataset from the *Tabula Muris (*Tabula Muris et al., 2018*)*. We observed that two main factors critical for CHIKV infection *in vivo,* MXRA8 *(*Zhang et al., 2018*)* and FHL1 *(*Meertens et al., 2021*)*, have increased expression in cardiac fibroblasts ($P < 0.001$, logistic regression model; **Figure 2B upper panel**) compared to other cardiac cell types included in the dataset. Indeed, *Mxra8* and *Fhl1* transcripts are co-expressed in 75% of cardiac fibroblasts **(Figure 2B, bottom panel)**, suggesting that cardiac fibroblasts may be the primary cardiac cell type infected by CHIKV. To test this hypothesis, hearts were harvested at 2 dpi, fixed, and serial cryosections were processed for staining with markers for different cardiac cell types: CD31 (endothelial cells), CD45 (leukocytes), αSMA (smooth muscle cells, pericytes, and myofibroblasts), cTnT (cardiomyocytes), and vimentin. Of note, vimentin is expressed at high levels in cardiac fibroblasts (Camelliti et al., 2005) but can also be expressed in smooth muscle cells, endothelial cells, and macrophages (Ivey and Tallquist, 2016; Lane et al., 1983; Tarbit et al., 2019). Therefore, we identified cardiac fibroblasts cells as vimentin^{+}/αSMA^{-}/CD31^{-}/CD45^{-} populations, a combination that we

orthogonally validated via single-cell RNA expression from the *Tabula Muris* (**Figure 2C**). By using confocal microscopy and co-localization analysis with the different cell type markers, we found that the CHIKV-ZsGreen signal colocalized with 78.5% of vimentin^{+}/αSMA^{-} cells **(Figure 2E)** suggestive of either cardiac fibroblasts, leukocytes or endothelial cells. This result, together with the reduced colocalization between CHIKV-ZsGreen signal and markers for endothelial cells (CD31^{+}; 7.3%), leukocytes (CD45^{+}; 7.2%), smooth muscle/pericytes/myofibroblasts (αSMA^{+}; 1%), and cardiomyocytes (cTnT^{+}; 4.4%; **Figure 2E and Figure S1E-G)** demonstrate that the cardiac fibroblasts are the primary target of CHIKV in infection in cardiac tissue.

Cardiac tissue clears CHIKV infection without inducing cardiac damage in WT mice. To explore how the heart responds to CHIKV infection, we first measured the kinetics of CHIKV infection in the heart. Significant levels of CHIKV RNA can be detected in the cardiac tissue of intravenously infected mice as early as 12 hours post-infection (hpi) with a peak at 2 dpi, and the infection is cleared out to background detection levels by 9 dpi **(Figure 3A, left panel)**. Infectious particles follow a similar trend, with a peak of infectious particle production between 1 and 2 dpi, and no

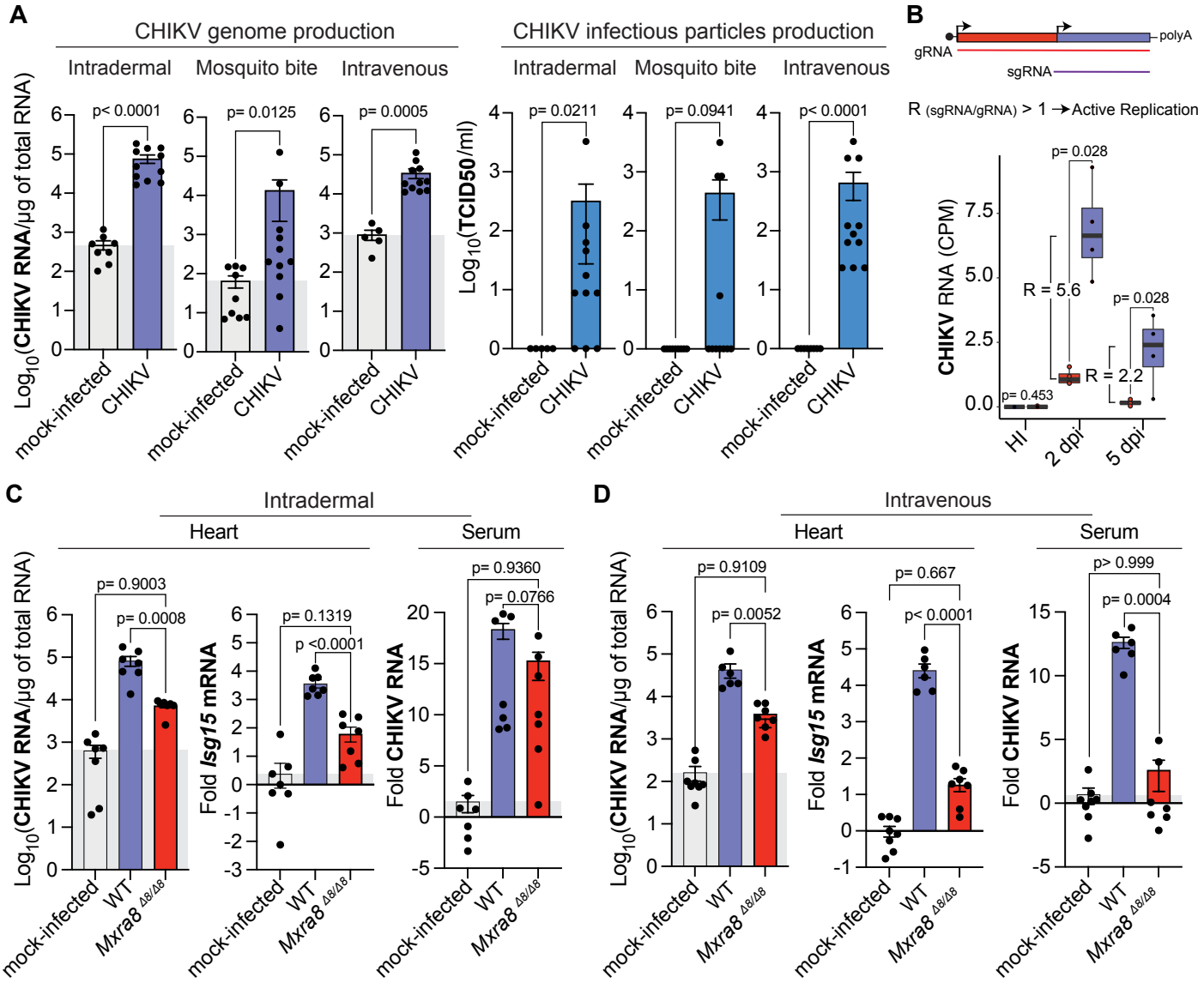

Figure 1. Cardiac tissue is infected by CHIKV in a MXRA8-dependent manner. A. Six-week-old C57BL/6 mice were inoculated with 10^5 PFU of CHIKV or mock-infected with PBS intradermally or intravenously; or infected via natural transmission through a mosquito bite. Infected tissue was extracted at 2 dpi for intradermal and intravenous infected mice, and at 2 and 3 dpi for mice infected through mosquito bite. Hearts were perfused with 30 ml of cold PBS. Viral genomes were quantified using RT-qPCR and infectious particles by $TCID_{50}$ in BHK-21 cells. **B.** Number of reads mapping to either the CHIKV sub-genomic (sgRNA, purple) or CHIKV genomic (gRNA, red) region in counts per million reads (CPM). The ratios (R) of normalized sgRNA to gRNA reads are shown. R > 1 indicates active viral replication. HI = heat-inactivated CHIKV. **C-D.** Differential CHIKV cardiac infection susceptibilities between *Mxra8*$^{D8/D8}$ and WT mice at 2 dpi. Mice were infected intradermally via footpad injection **(C)** or intravenously **(D)** with 10^5 PFU of CHIKV or CHIKV-ZsGreen reporter virus, respectively. Viral genomes and *Isg15* expression levels were measured by RT-qPCR. P values were calculated using Mann-Whitney test **(A-B)**, or Kruskal-Wallis test **(C-D)**. Data represent two to three independent repetitions with a total of 6 to 11 mice per group. Gray boxes represent the background levels corresponding to the mock-infected mice. See also Figure S1.

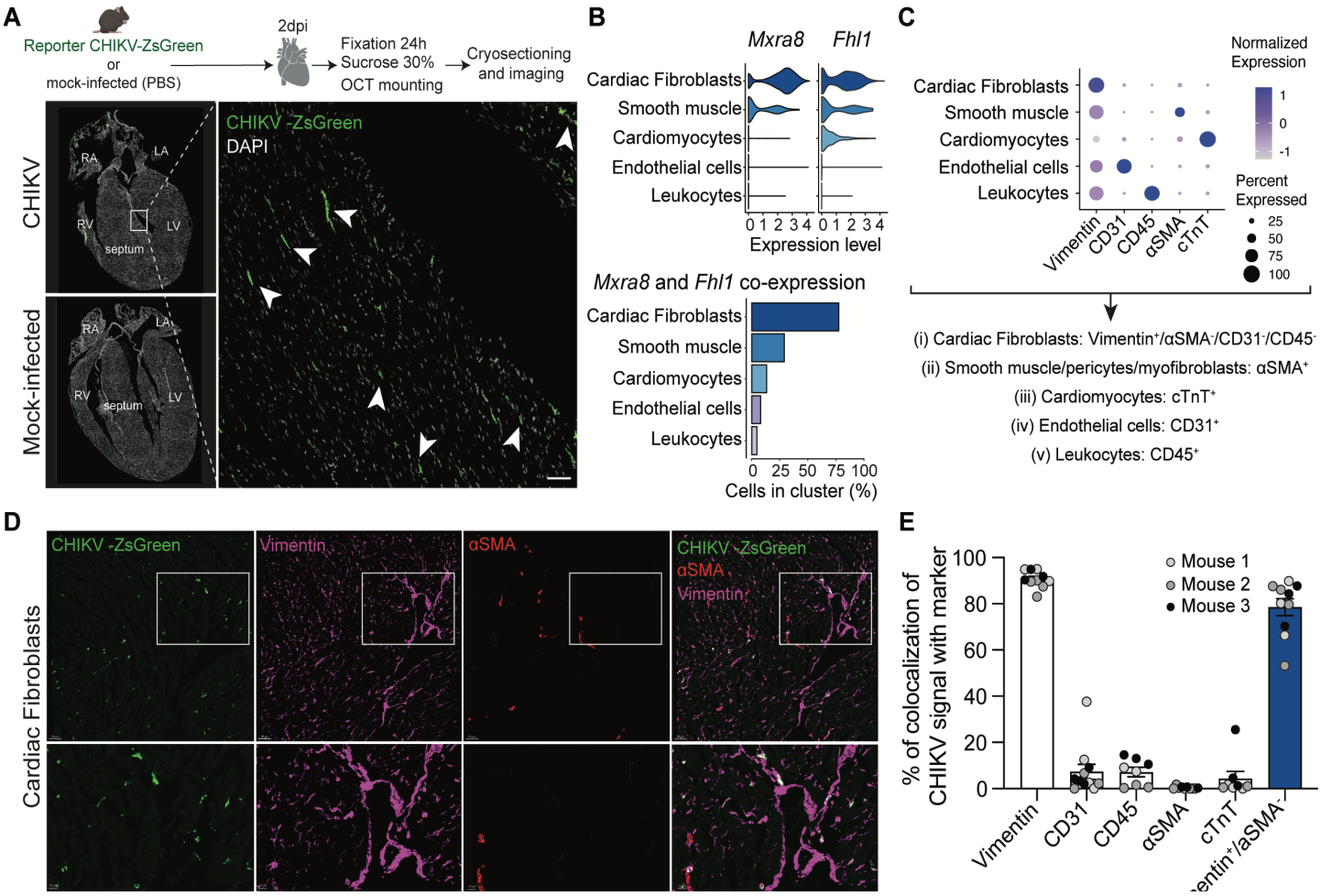

Figure 2. Cardiac fibroblasts are the main target of CHIKV infection in infected hearts. A. Upper panel: Schematic representation of the experimental setup. Mice were inoculated intravenously with 10^5 PFU of reporter CHIKV-ZsGreen or mock-infected with PBS. Bottom panel: Whole heart sections showing 4 chamber-view. Green channel: CHIKV-infected cells. Gray channel: DAPI. White arrows: CHIKV-infected cells. (scale = 50 µm). **B.** Expression (upper panel) and co-expression (bottom panel) of *Mxra8* and *Fhl1* by cell types in murine hearts using the *Tabula Muris* data set (Tabula Muris et al., 2018). Bar graphs represent the percentage of cells from each cell type co-expressing both *Mxra8* and *Fhl1*. **C.** Dot plot showing the expression levels of the markers used in the study by cardiac cell type. Bottom schematics: strategy for cell-type identification. **D.** Representative immunofluorescence images of ventricular sections of CHIKV-infected hearts. The panel represents the individual channels for reporter CHIKV-ZsGreen (green), vimentin (violet), and αSMA (red), or merge (white) (top scale = 50 µm and bottom scale = 15 µm). **E.** Co-localization analysis between CHIKV-infected cells and different cell type markers. Data are represented as the percentage of the total of green signal (infected cells) overlapping with the indicated markers. Colocalization analysis was done in three to four fields for three different infected mice (black, open and gray dots). See also Figure S1.

detectable levels by 9 dpi **(Figure 3A, right panel)**. Comparable results were obtained by measuring CHIKV-positive cells in infected hearts by fluorescent microscopy, with no detectable ZsGreen positive cells by 7dpi **(Figure 3B)**. Interestingly, albeit with higher CHIKV RNA levels, the viral replication kinetics follow a similar temporal pattern when measured in calf muscle, a bonafide primary organ of CHIKV replication **(Figure S2A)**. Altogether, these results demonstrate that cardiac tissue efficiently clears CHIKV infection.

Cellular infiltration mediated by inflammatory factors at the site of infection is a hallmark of CHIKV pathogenesis (Long and Heise, 2015). By performing multiplex cytokine analysis on infected cardiac tissue homogenates, we confirmed that CHIKV infection in the heart induces proinflammatory cytokine and chemokine (CCL2, CCL5, CCL3, TNFα, IL6, IFNγ, IL2, KC, IL1α, IL12p70, and IL12p40) production at 2 dpi. However, IL12p40 is the only cytokine that remains upregulated at 5 dpi **(Figure 3C-D, and Figure S2B-D)**, indicating that CHIKV infection is inducing a transient inflammatory state in cardiac tissue. Quantification of $CD45^+$ cells at 2 or 5 dpi by immunofluorescence **(Figure 3E)** revealed no visible mononuclear cell infiltrates in ventricles, septum, or atria of CHIKV-infected hearts. Similar results were observed by histopathological analysis of hematoxylin-eosin (H&E) staining of four-chamber view sections of infected and mock-infected at 3, 5, 10, 15, and 30 dpi **(Table S1).** Interestingly, focal endothelialitis consisting of mononuclear cells was present in the aorta (Ao) and the pulmonary artery (PA) in 1 out of 3 mice at 10 dpi, and in 1 out of 5 mice at 15 dpi, respectively (**Figure S3 and Table S1)**. These results suggest that cardiac tissue is clearing CHIKV infection without notable mononuclear cell infiltration in the myocardium.

Elevated cardiac troponins have been observed in individuals with CHIKV-associated cardiac manifestations (Cotella et al., 2021; Farias et al., 2019; Gasque et al., 2016; Hsu et al., 2019). Therefore, to define whether CHIKV can lead to cardiac tissue

damage in mice, we evaluated the serum levels of cardiac troponin-T (cTnT) at 2 and 5 dpi by ELISA. We did not observe significant differences in levels of cardiac troponin-T in serum between infected and mock-infected control (**Figure 3F**), suggesting that CHIKV replication does not induce damage to cardiomyocytes. To further address direct cardiac damage, we assessed cardiac tissue apoptosis by performing immunohistochemistry (IHC) against cleaved caspase 3 (cleaved CASP3) of CHIKV-infected or mock-infected mice at 3 and 5 dpi. No differences in cleaved CASP3 levels were observed between infected and mock-infected mice **(Figure 3G).** Altogether, these results demonstrate that cardiac tissue can efficiently clear CHIKV infection without significant cardiac damage in WT mice.

CHIKV-infected cardiac tissue induces IFN-I signaling in both infected and non-infected cells. To understand how cardiac tissue rapidly clears CHIKV, we measured the transcriptional response of

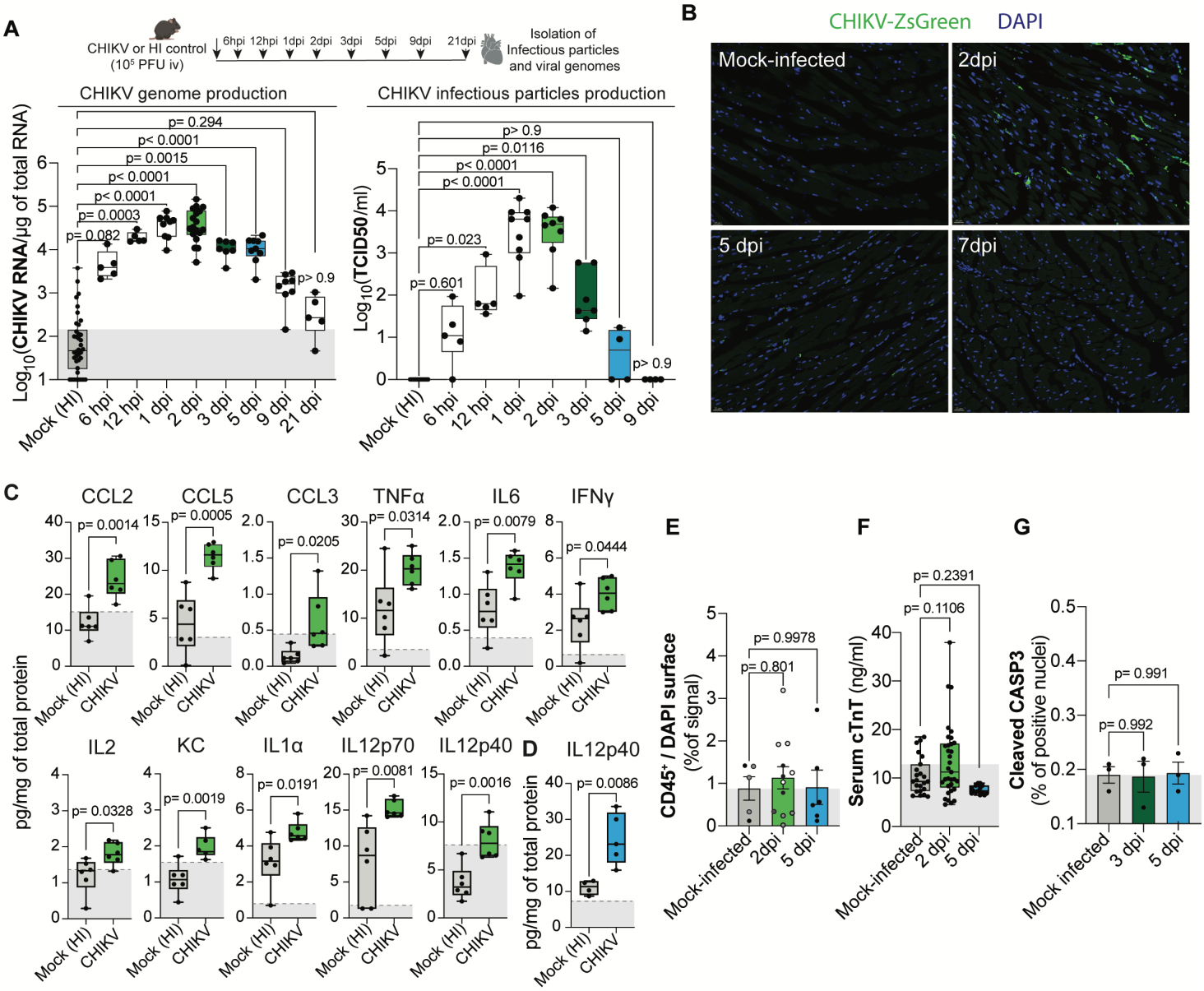

Figure 3. Cardiac tissue clears CHIKV infection without inducing cardiac damage in WT mice. A. CHIKV heart infection kinetics. Upper panel: Schematic representation of the experimental design. Bottom panel: CHIKV viral genomes or CHIKV infectious particles determined by RT-qPCR or $TCID_{50}$ in BHK-21 cells, respectively. N=5 to 9 mice per timepoint. **B.** Representative immunofluorescence images of ventricular sections of CHIKV-ZsGreen infected and mock-infected hearts (scale = 20 µm). **C-D.** Protein levels of significantly induced proinflammatory cytokines and chemokines in cardiac tissue homogenates measured by Bio-Plex Pro Mouse Cytokine 23-plex Assay at 2 dpi **(C)** and 5 dpi **(D)**. The dashed-gray box represents the detection limit for each protein determined as the last value in the calibration curve. N=5 to 6 mice per group. **E.** Co-localization analysis between $CD45^+$ cells and different DAPI staining. Mice were inoculated intravenously with 10^5 PFU of reporter CHIKV-ZsGreen or mock-infected with PBS, harvested at 2 dpi and cardiac tissue was stained with CD45 and DAPI. Data are represented as the percentage of the total $CD45^+$ cells overlapping with DAPI staining. The same color indicates different fields per section. Different colors indicate independent infected mice. **F.** Serum levels of cardiac troponin-T measured by ELISA. **G.** Quantifications of cleaved CASP3 nuclei versus total nuclei were performed in whole ventricular sections (LV, RV, and septum) using Visiopharm^R. Each dot represents one individual mouse (N=3 mice/group). P values were calculated using Kruskal-Wallis test **(A, E-G)** or using Mann Whitney test **(C and D)**. Gray boxes represent the background levels corresponding to the mock-infected mice **(A, E-G)**. See also Figure S2-S3, and Table S1.

CHIKV-infected heart homogenates by bulk RNA-seq. We used CHIKV-infected mice at 2 dpi (where we detect both RNA and infectious particles) or at 5 dpi (where little to no infectious particles, but still significant viral RNA levels are detected (**Figure 3A**). To identify changes derived only from active CHIKV replication, we used the HI virus as a control. Principal component analysis (PCA) showed that biological replicates grouped by treatment (**Figure S4A**). A total of 377 upregulated genes and 84 downregulated genes were detected at 2 dpi, and 259 upregulated genes as well as 52 downregulated genes at 5 dpi **(Figure 4A, Figure S4B, and Table S2-S3)**. The top-10 upregulated genes on both days include genes associated with protection of cardiac tissue damage and mitochondria metabolism (*Apod*, *Atf5, Mthfd2*) (Tsukamoto et al., 2013; Wang et al., 2019), IFN-I response (*Ifi27*, *Ddx60, Serping1*), cytokine signaling

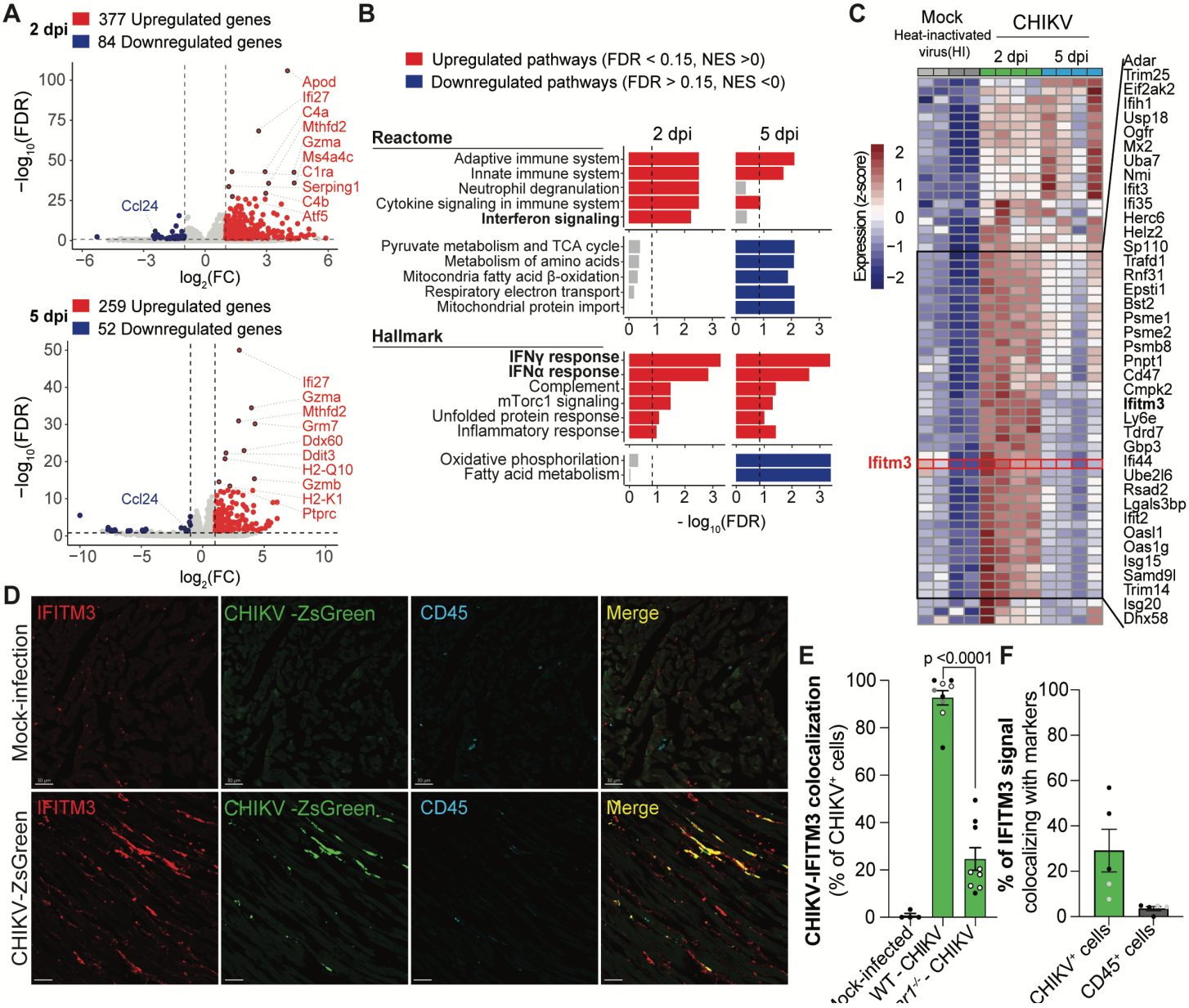

Figure 4. CHIKV-infected cardiac tissue induces IFN-I signaling in both infected and non-infected cells. A. Volcano plots from differential expression analysis at 2 dpi (top panel) and 5 dpi (bottom panel). Red and blue indicate upregulated (FDR < 0.15 and log_2FC > 1) and downregulated genes (FDR < 0.15 and log_2FC < -1), respectively. Top-10 differentially expressed genes are indicated. N=4 mice/group. **B.** GSEA pathway enrichment analysis for Reactome, and Hallmark datasets showing top upregulated (FDR < 0.15 and normalized enrichment score (NES) > 0, red bars) and downregulated (FDR < 0.15 and NES < 0, blue bars) pathways at 2 dpi and 5 dpi. **C.** Heat map showing the differentially expressed genes (FDR < 0.15) from the Hallmark IFNa response pathway for CHIKV-infected and mock-infected (HI) hearts. Black box highlights a subset of genes of interest. *Ifitm3* gene is highlighted in red. **D.** Immunofluorescence images of ventricular sections of CHIKV-infected hearts and mock-infected control (PBS) at 2 dpi. Red: IFITM3. Green: CHIKV-ZsGreen infected cells. Cyan: $CD45^+$ cells. Yellow: co-localization of infected cells with IFITM3 marker (scale = 30 µm). **E.** Co-localization analysis between CHIKV-infected cells and IFITM3 marker for WT and *Ifnar1*$^{-/-}$ infected mice. WT and *Ifnar1*$^{-/-}$ mice were inoculated intravenously with 10^5 PFU of reporter CHIKV-ZsGreen or mock-infected with PBS, harvested at 2 dpi and cardiac tissue was stained with IFITM3. Data are represented as the percentage of the total of infected cells overlapping with the IFITM3 maker. Colocalization analysis was done in three to five independent sections for two to three different infected mice (WT: black, open and gray dots; *Ifnar1*$^{-/-}$: black and open dots). Mock-infected mice were measured to establish the background level. P values were calculated using Mann-Whitney. **F.** Percentage of the total IFITM3 signal overlapping with either CHIKV-ZsGreen or $CD45^+$ cells. Colocalization analysis was done in two to three independent sections for 2 different infected WT mice (black and gray dots). See also Figure S4, and Table S2-S4.

(*H2-K1*), and complement cascade (*C4a*, *C4b, C1ra*) **(Figure 4A)**. In line with these observations, GSEA pathway enrichment analysis for Reactome and Hallmark datasets show upregulation (FDR < 0.15 and normalized enrichment score [NES] > 0) of several pathways associated with innate immunity, adaptive immunity, IFN signaling **(Figure 4B and Table S4)**. Downregulated pathways (FDR < 0.15 and NES < 0) in infected heart homogenates at 5 dpi include metabolic pathways such as metabolism of amino acids, respiratory electron transport, and oxidative phosphorylation, among others **(Figure 4B and Table S4)**.

The induction of IFN-I signaling pathways in non-hematopoietic cells is essential to control CHIKV infection in mammals (Schilte et al., 2012; Schilte et al., 2010). We found that the IFN-I pathway is significantly induced in CHIKV-infected hearts at both 2 and 5 dpi (**Figure 4C and Figure S4C**). Particularly, we observed upregulation of ISGs (e.g. *Isg15, Ifitm3, Mx1, Mx2, Ifit1, Ifit2, Ifit3, ifi27*, *Ddx58,* and *Ddx60,* among others) as well as genes involved in the IFN-I signaling pathway (e.g. *Irf7, Stat1, Stat2*; **Table S2 and Table S3)**.

To gain insight into whether the IFN-I response observed by RNA-seq was locally mediated by infected cardiac cells, we looked at the induction of IFITM3*,* an ISG that restricts CHIKV infection (Poddar et al., 2016), and that is upregulated at 2 dpi in CHIKV-infected hearts **(Figure 4C, red**). Quantification of the overlapping signal between IFITM3 and CHIKV-ZsGreen positive signal revealed that 95% of CHIKV-infected cells are positive for the IFITM3 marker (**Figure 4D-E**). While IFITM3 is expressed at basal levels in the absence of interferon induction, its expression is highly induced by either IFN-I or interferon-γ (Diamond and Farzan, 2013). We found that in the absence of the IFN-I receptor (interferon a/b receptor – IFNAR)) only 24.6% of CHIKV-infected cells colocalize with the IFITM3 signal **(Figure 4E)**, demonstrating that the observed response is partially dependent on IFN-I. Moreover, 29.1% of the total IFITM3 positive signal corresponds to CHIKV-infected cells **(Figure 4F)**, suggesting that CHIKV infection is establishing a robust antiviral state in cardiac tissue. Finally, to define if cardiac leukocytes ($CD45^+$) were responding to IFN-I, we analyzed the colocalization between CD45 and IFITM3 makers. We observed only 3.56% of colocalization between CD45 and IFITM3 makers **(Figure 4F)**, demonstrating that non-hematopoietic cells are the major responders to the IFN-I in CHIKV-infected hearts. Altogether, these results demonstrate that cardiac tissue mounts a robust and local IFN-I response upon CHIKV infection.

IFN-I signaling pathway restrains CHIKV cardiac infection, preventing viral spreading and cardiac tissue damage. To determine the contribution of the IFN-I response in controlling CHIKV heart infection, we infected interferon a/b receptor-deficient mice (*Ifnar1*$^{-/-}$) and WT mice intravenously with CHIKV (**Figure 5A, upper panel**). We observed that in the absence of IFN-I signaling, CHIKV genome and infectious particle production are significantly increased in cardiac tissue compared to WT mice **(Figure 5A)**. This increase in infectious particle production was also observed in the calf muscle, a primary site of CHIKV infection, but not observed in a non-CHIKV-target organ such as the pancreas **(Figure 5A)**. In addition, we performed confocal microscopy of cardiac tissue from CHIKV-ZsGreen infected *Ifnar1*$^{-/-}$ or WT mice, and found that *Ifnar1*$^{-/-}$ showed a more spread infection compared to WT mice **(Figure 5B)**. These results support that the IFN-I response controls the spreading of CHIKV infection in cardiac tissue. Intriguingly, while cardiac fibroblasts ($Vimentin^+/aSMA^-$; 42%) still represent the primary target of CHIKV infection in cardiac tissue in *Ifnar1*$^{-/-}$ mice **(Figure 5C)**, we observed an increased population of endothelial ($CD31^+$; 16.5%) and smooth muscle (αSMA^+; 6.3%) infected cells (**Figure 5D)** relative to WT (**Figure 2E**). This is concordant with an observed increase in infection around heart vessels (**Figure 5C and Figure S5**).

Next, we asked whether the observed increased infection in *Ifnar1*$^{-/-}$ mice results in cardiac damage. For that purpose and since CHIKV-infected *Ifnar1*$^{-/-}$ mice succumb to the infection at ~ 2 dpi, we assessed cardiac tissue apoptosis by cleaved CASP3 staining at 1 dpi. We observed that while infection of WT mice showed similar levels of cleaved CASP3 signal in comparison to mock-infected control, *Ifnar1*$^{-/-}$ mice showed a significantly increased level of cleaved CASP3 within the ventricular region (RV, LV, and septum; **Figure 5E)**. Altogether, these results demonstrate that a robust IFN-I response is essential to control CHIKV infection in the heart and prevent cardiac tissue damage.

MAVS signaling contributes to CHIKV clearance, and prevents major vessel vasculitis, and cardiac tissue damage in CHIKV-infected hearts. IFN-I signaling is triggered upon recognition of CHIKV RNA via either cytosolic (RIG-I/MDA5) or endosomal receptors (TLR3/7) (Fox and Diamond, 2016). To gain insight into the mechanisms of how cardiac tissue clears CHIKV infection, we took advantage of mice deficient in major innate immune signaling components including MYD88, TRIF, or MAVS. In addition, to address for the contribution of the NLRP3 inflammasome in CHIKV clearance (Chen et al., 2017; Ekchariyawat et al., 2015) we used CASPASE 1/11 deficient mice. We infected each mouse intravenously with CHIKV and evaluated viral burden in cardiac tissue at 2, 5, and 7 dpi. We found no significant differences in the infection kinetics between *Myd88* $^{-/-}$, *Trif* $^{Lps2/Lps2}$ or *Casp1/11*$^{-/-}$ mice compared to WT mice **(Figure 6A)**, suggesting that CHIKV RNA sensing through neither TLR7, TLR3, nor inflammasome activation is involved in CHIKV clearance from infected cardiac tissue. Intriguingly, infectious particles were detectable up to 7 dpi for *Mavs*$^{-/-}$ mice **(Figure 6A)**. When we expanded our analysis up to 15 dpi, we found that infectious particles can be detected up to 10 dpi

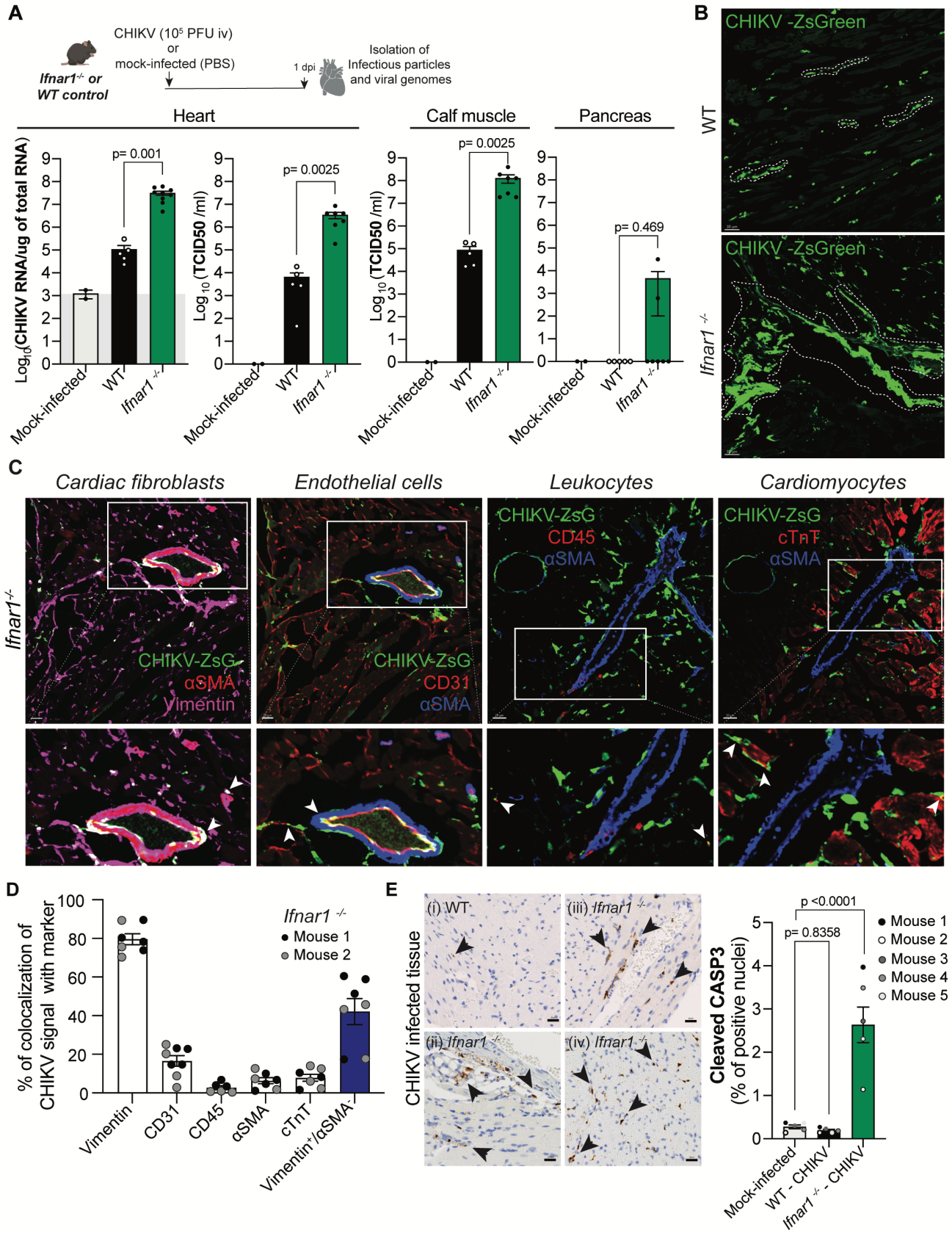

Figure 5. IFN-I pathway restrains CHIKV heart infection, preventing viral spreading and cardiac tissue damage. A. WT or *Ifnar1*$^{-/-}$ mice were infected intravenously with 10^5 PFU of CHIKV or mock infected with PBS. CHIKV viral genomes were determined by RT-qPCR and infectious particles by $TCID_{50}$ in BHK-21 cells. Mock-infected (N= 2), CHIKV-infected WT or *Ifnar1*$^{-/-}$ (N= 5 to 7 mice per group). **B.** Representative immunofluorescence images of CHIKV-ZsGreen WT or *Ifnar1*$^{-/-}$ infected hearts at 2 dpi. White shapes highlight CHIKV infection spreading (scale = 30 µm). **C.** Representative immunofluorescence images of ventricular sections of *Ifnar1*$^{-/-}$ infected hearts (scale = 30 µm). Arrows highlight the co-localization between the different markers. **D.** Percentage of the total of infected cells (green signal) overlapping with the indicated makers. Co-localization analysis was done in three to four independent sections for two different infected mice (black and gray dots). **E.** Apoptosis staining was measured by immunohistochemistry against cleaved CASP3 (scale = 50 µm). Arrows highlight apoptotic foci. Quantifications of cleaved CASP3 nuclei versus total nuclei were performed in whole ventricular sections (LV, RV, and septum) using Visiopharm^R. Each dot represents one individual mouse (N=5 mice/group). P values were calculated using Mann-Whitney or Kruskal-Wallis test (**A and E, respectively**). See also Figure S5.

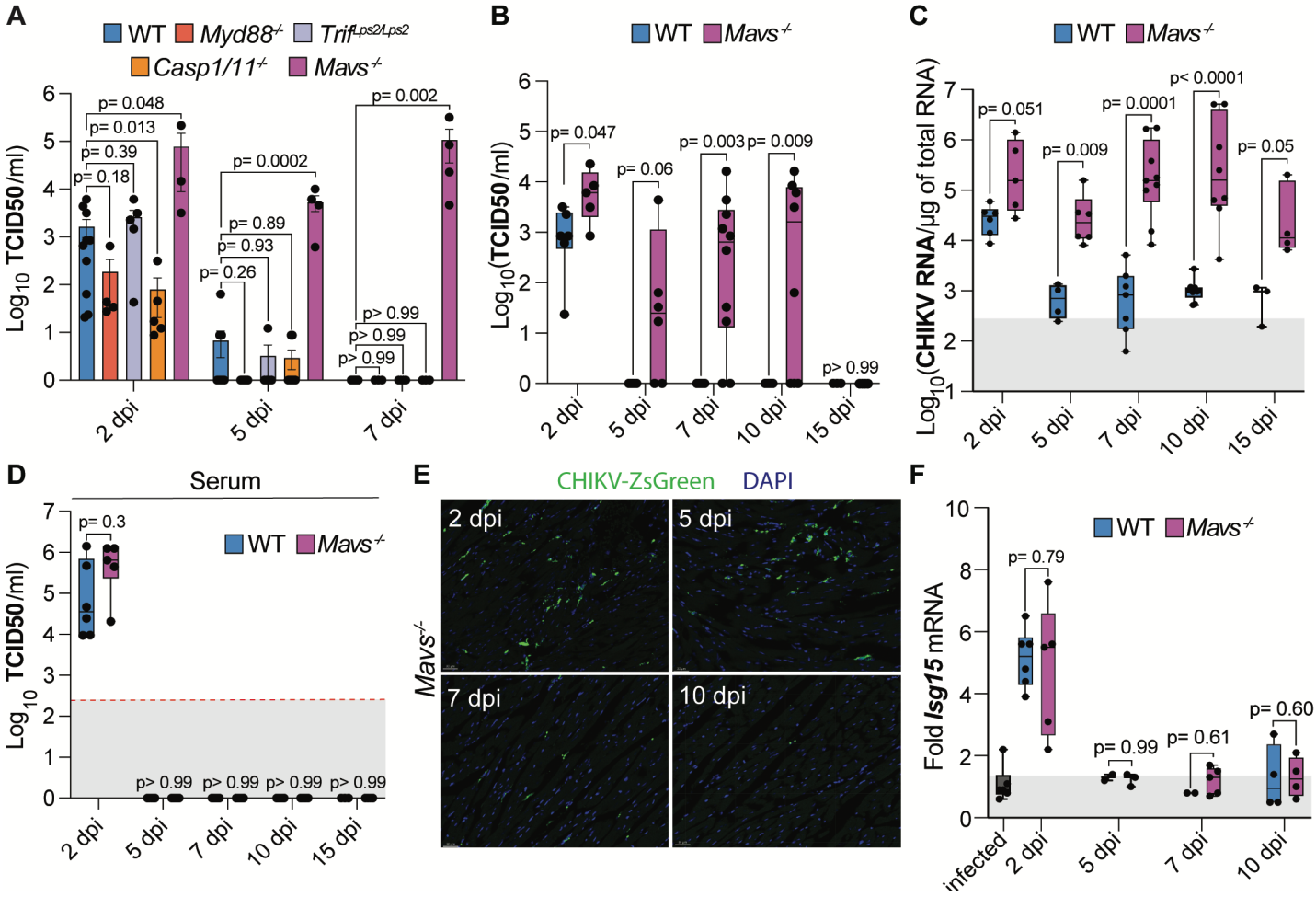

Figure 6. MAVS signaling regulates CHIKV clearance in CHIKV-infected hearts. **A.** Differential CHIKV cardiac infection susceptibilities between *MyD88*$^{-/-}$, *Trif*$^{Lps2/Lps2}$, *Casp1/11*$^{-/-}$, *Mavs*$^{-/-}$, and WT mice at 2, 5, and 7 dpi. Mice were infected intravenously with 10^5 PFU of CHIKV. CHIKV infectious particles were determined by $TCID_{50}$ in BHK-21 cells. **B-C.** CHIKV cardiac infection kinetics in *Mavs*$^{-/-}$ and WT mice. CHIKV infectious particles from heart homogenates were determined by $TCID_{50}$ in BHK-21 **(B)**. CHIKV viral genomes were determined by RT-qPCR **(C)**. **D.** CHIKV infectious particles from serum determined by $TCID_{50}$ in BHK-21. **E.** Representative immunofluorescence images of ventricular sections of CHIKV-ZsGreen infected *Mavs*$^{-/-}$ hearts (scale = 30 µm). **F.** Dynamics of *Isg15* expression levels in *Mavs*$^{-/-}$ and WT infected hearts. P values were calculated using Mann-Whitney (**A-D, and F**). N= 5 to 10 mice per condition. See also Figure S6.

(Figure 6B) and CHIKV viral RNA was consistently detected up to 15 dpi **(Figure 6C)**. Moreover, infectious particles in serum were cleared by 5 dpi for both *Mavs*$^{-/-}$ and WT mice **(Figure 6D)**, suggesting that the delay in the clearance of CHIKV infection is tissue specific. In line with this, CHIKV-ZsGreen infectious foci were detected up to 10 dpi in infected hearts **(Figure 6E)**. Collectively, these results demonstrated that sensing through MAVS is playing a central role in the clearance of CHIKV infection from cardiac tissue. Of note, we found that *Mavs*$^{-/-}$ infected hearts induced similar levels of *Isg15* mRNA compared to WT **(Figure 6F)**. This suggests that the delay in CHIKV clearance cannot be entirely explained by a reduced IFN-I induction associated to *Mavs*$^{-/-}$.

Finally, we asked whether the delay in CHIKV clearance can lead to cardiac tissue damage. We infected *Mavs*$^{-/-}$ and WT mice and harvested the heart for histopathological analysis at 10, 15, and 30 dpi **(Table S1 and S5)**. Focal and multifocal myocarditis accentuated around the vessels was present and characterized by CD11b$^+$ and CD3$^+$ cell infiltrates in 4 out of 6 CHIKV-infected *Mavs*$^{-/-}$ mice at 15 dpi and 2 out of 5 at 30 dpi **(Figure 7A-B)**. In addition, a fraction of mice developed focal inflammation in the right atria (RA) endocardium at 10 dpi and 15 dpi **(Table S5)**. Quantification of the number of CD3$^+$ cells in LV, RV and septum confirmed a significant increase of CD3$^+$ at 15 dpi compared to WT, which started to wean by 30 dpi **(Figure 7C)**. Moreover, all the infected mice from the *Mavs*$^{-/-}$ group developed vasculitis involving the Ao and PA characterized by CD3$^+$ and CD11b$^+$ cell infiltrates (**Table S5 and Figure 7D)**. Vasculitis was identified as early as 10 dpi and remained detectable at 30 dpi **(Figure 7E)**. Of note, while both WT and the *Mavs*$^{-/-}$ mice showed vasculitis, *Mavs*$^{-/-}$ mice had transmural inflammation of the vessel wall **(Figure 7D)**, whereas in the WT mice only endothelialitis was observed **(Figure S3B-C)**. Interestingly, serum levels of cTnT remain stable (**Figure S6**). Altogether, these results demonstrate that persistence of CHIKV infection in cardiac tissue can lead to inflammatory infiltrates leading to focal or multifocal myocarditis and big vessel cell vasculitis, and demonstrates that MAVS signaling is essential to control CHIKV infection in the heart and prevent cardiac tissue damage.

DISCUSSION

It is established that cardiac complications account for more than 20% of CHIKV-associated

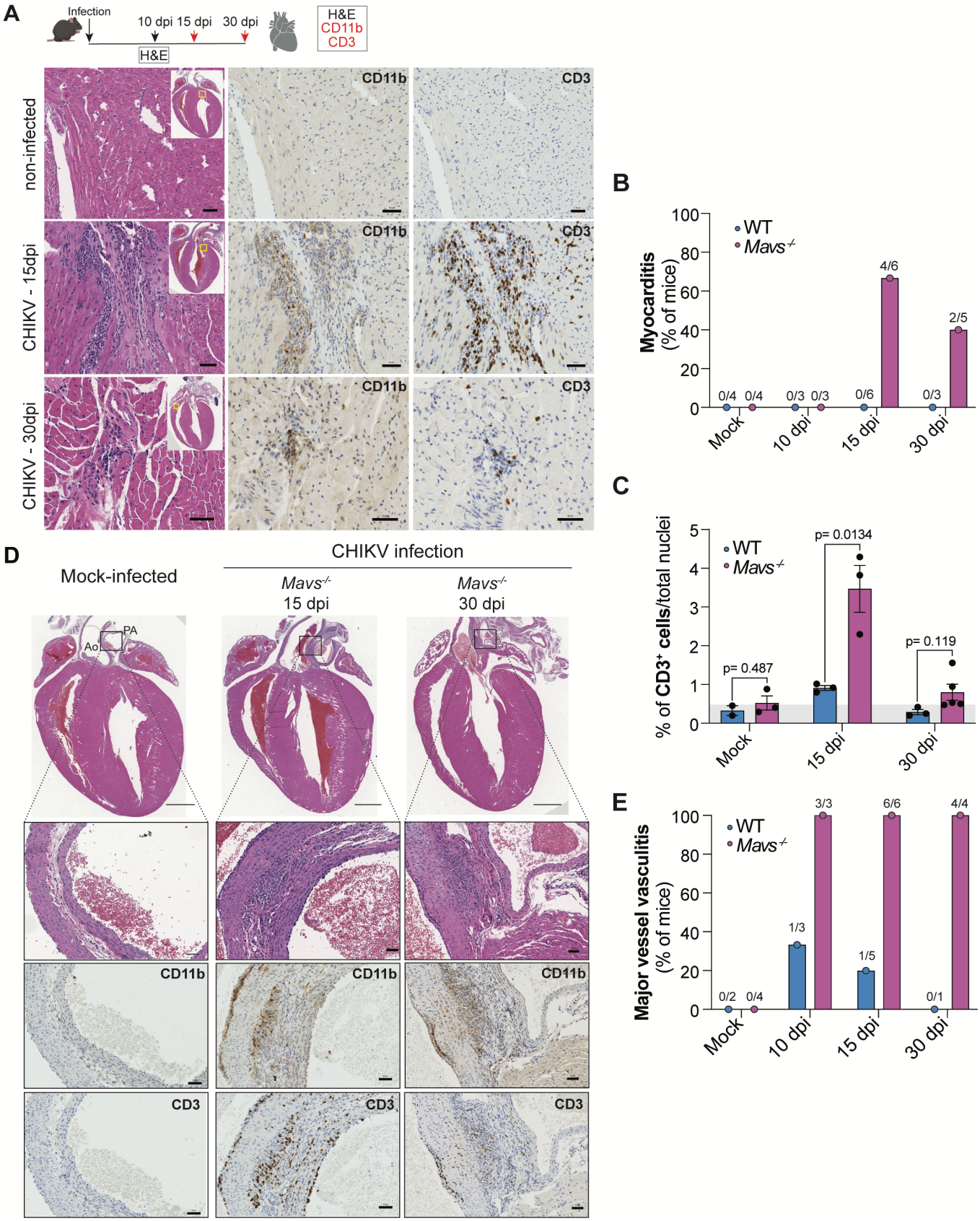

Figure 7. *Mavs*$^{-/-}$ mice develop myocarditis and big vessel vasculitis upon CHIKV infection. **A.** Upper panel: Schematic representation of the experimental design. Bottom panel: Representative H&E, CD11b and, CD3 staining for CHIKV or mock-infected *Mavs*$^{-/-}$ at 15 dpi and 30 dpi (scale = 50 µm). Inset shows the four-chamber view representation. The yellow square indicates the section selected. **B.** Quantification of number of mice with positive signs of myocarditis. Data represent the percentage of mice with any sign of myocarditis over the total amount of mice analyzed (related to **Table S1 and Table S5**). **C.** Quantifications of CD3^{+} cells over total nuclei were performed in whole ventricular sections (LV, RV, and septum) using Visiopharm^{R}. Each dot represents one individual mouse (N=2-5 mice/group). **D.** Upper panel: H&E showing four-chamber view and major vessels at the base of the heart. Representative pulmonary arteries (PA) images for 15 dpi and 30 dpi CHIKV-infected hearts for *Mavs*$^{-/-}$. Bottom panel: magnification of the PA sections for H&E, CD11b and CD3 staining. **E.** Quantification of number of mice with major vessel vasculitis. Data represent the percentage of mice with any sign of vasculitis over the total amount of mice analyzed (related to **Table S1-S5 and Figure S3**). P values were calculated using Multiple unpair t-test (**C**). See also Figure S3 and Tables S1 and S5.

deaths (de Lima et al., 2021; Sharp et al., 2021; Traverse et al., 2021). Here, we demonstrate that cardiac tissue, in particular cardiac fibroblasts, is a direct target of CHIKV infection. In addition, we showed that infected cardiac tissue elicits a robust and local IFN-I response arising from non-hematopoietic cardiac cells, and loss of the IFN-I pathway results in increased CHIKV infection, virus spreading, and apoptosis in cardiac tissue. Finally, we demonstrated that MAVS signaling is essential for CHIKV clearance from infected hearts, and that failure to clear CHIKV can lead to major vessel vasculitis and focal myocarditis.

Previous studies, including our own, reported the presence of infectious particles or viral RNA in the cardiac tissue of CHIKV-infected mice (Clavarino et al., 2012; Langsjoen et al., 2021; Noval et al., 2019). However, in these studies, mice were not perfused, thus confounding measurements due to the potential presence of the virus originating from serum in CHIKV-infected hearts. Here, by including a perfusion step, we show that CHIKV can disseminate, replicate and generate infectious particles in cardiac tissue in WT mice regardless of the inoculation route of CHIKV (via mosquito bite, intradermal, or intravenous injection). Moreover, we show that CHIKV infects cardiac fibroblasts and that its infection follows a discrete and focalized pattern within ventricles, atria, valves, and the perivascular region. CHIKV antigen in cardiac fibroblasts was previously identified in human necropsies of individuals who died from CHIKV (Sharp et al., 2021) and thus supports a similar tropism observed in humans. Indeed, both human and murine cardiac fibroblasts show high levels of expression of the CHIKV receptor Mxra8 (Cotella et al., 2021). The significant reduction in CHIKV genomes isolated from *Mxra8*$^{D8/D8}$ infected hearts, in addition to the significant levels of *Mxra8* expression in cardiac fibroblasts, suggests that CHIKV heart infection is mediated in part by the expression of the CHIKV receptor Mxra8 (Zhang et al., 2018).

We found that in WT mice CHIKV is cleared from cardiac tissue within the first week of infection without causing tissue damage. Indeed, our RNA-seq data revealed that infected cardiac tissue shows upregulation of innate immunity, adaptive immunity, and IFN-I signaling pathways, similar to what has been described for footpad and lymph node CHIKV-infected tissue (Wilson et al., 2017). In addition, we found that genes previously associated with cardioprotection and antioxidant metabolism (*Apod, Aft5, Fgf21, and Mthfd2*) were upregulated at 2 dpi (**Table S2**) (Fan et al., 2014; Planavila et al., 2015). *Apod* is a cardioprotective gene whose expression is induced in mouse hearts during myocardial infarction and has been proposed to protect the heart against ischemic damage (Tsukamoto et al., 2013). In addition, *Apod* has been reported to be the most significantly upregulated gene in SARS-CoV-2-infected cardiac tissue in fatal COVID-19 cases (Brauninger et al., 2022) and has been found upregulated in a cluster of cardiac fibroblasts during Coxsackievirus B3 infection (Lasrado et al., 2022). Further studies are required to determine the specific role of *Apod* in cardioprotection during CHIKV infection.

Intriguingly, using the KEGG datasets we observed upregulation of the viral myocarditis pathway and downregulation of cardiac tissue contractility pathway at 5 dpi **(Figure S4D-G and Table S4)**. However, we did not observe any sign of cardiac tissue damage by histopathology (**Figure 3**), suggesting that CHIKV infection is triggering transcriptional programs involved in cardiac dysfunction that are not sufficient to result in overt phenotypes of cardiac damage. We found that CHIKV-infected hearts display a significant yet transient production of proinflammatory chemokines and cytokines. Interestingly, it has been shown that upon TLRs or RIG-I-like receptor stimulation, human cardiac fibroblasts can produce proinflammatory cytokines and induce an antiviral immune response (Li et al., 2021). Therefore, the CHIKV-infected cardiac fibroblasts may be contributing to this transient production of immune modulators. Indeed, we did not observe mononuclear cell infiltration in cardiac tissue by H&E, or by immunofluorescent staining against CD45 cells **(Figure 3)**. Taken together, our results support the idea that in the context of an immunocompetent host, the infected cardiac tissue mounts a robust and local IFN-I response resolving CHIKV infection within few days, with little to no cardiac damage. This suggests a possible explanation of why CHIKV cardiac manifestation is not a pervasive outcome in CHIKV-infected individuals. One limitation of this study is that bulk population measurements might occlude local cellular effects. Single-cell technologies have been recently applied to the study of cardiac tissue, providing the opportunity to study viral myocarditis at single-cell resolution (Lasrado et al., 2022). Further studies focusing on spatial single-cell transcriptomics on CHIKV-infected cardiac tissue may help elucidate the role of the local inflammation in CHIKV clearance.

Our RNA-seq analysis revealed that the infected cardiac tissue induces a robust IFN-I response upon CHIKV infection. In addition, 95% of infected cells co-localized with the IFITM3 marker and represent 29.1% of the total IFITM3 expressing cells. While in cardiac tissue basal levels of *Ifitm3* are expressed at steady-state (Tabula Muris et al., 2018), the increased levels of IFITM3 expression during infection in comparison to the mock-infected controls strongly suggest that non-infected cells respond to IFN-I in a paracrine manner. Thus, an inflammatory microenvironment potentially contributes to the clearance of the infection. Indeed, our results demonstrate that in the absence of an IFN-I response, the number of infectious particles and genomes, the extension of the viral spreading, and cardiac tissue damage are significantly increased in comparison to WT. In line with this, a report using knock-out (KO) mice for a protein implicated in the production of IFN-β during CHIKV infection (GADD34) revealed a significant increase in viral particles in the heart and cardiac inflammation compared to WT (Clavarino et al., 2012). Similar results were described for IFITM3 KO

mice during influenza virus infection (Kenney et al., 2019). Therefore, we can speculate that genetic and non-genetic factors (such as co-infections, diet, among others) that lead to a reduced IFN-I response could increase the risk of cardiac complications in CHIKV-infected patients. The link between the role of genetic polymorphisms in components from the IFN-I pathway in humans and susceptibility to viral infections has been reported (Ciancanelli et al., 2015; Zhang et al., 2020). Indeed, single nucleotide polymorphisms (SNPs) in TLR3 found in patients with enteroviral myocarditis have been associated with a decreased TLR3 mediated signaling and shown an impaired IFN-I response after Coxsackievirus B3 infection (Gorbea et al., 2010).

Multiple PRRs are involved in the *in vivo* control of CHIKV infection (Schilte et al., 2010). Here, we demonstrate that CHIKV clearance from infected tissue is MAVS-dependent, but independent of MYD88, TRIF, or the NLRP3 inflammasome. We demonstrate that in the absence of MAVS, CHIKV can generate infectious particles that persist in the cardiac tissue up to 10 dpi, and display significant amounts of CHIKV RNA compared to WT up to 15 dpi. Intriguingly, we found that in *Mavs*$^{-/-}$ mice, infected hearts display similar levels of *Isg15* compared to WT, suggesting that other pathways may also contribute to IFN-I response in cardiac tissue. This has been observed for Rift Valley fever virus-infected brains, in which no differences in the global induction of the IFN-I signaling between *Mavs*$^{-/-}$ and WT were observed by bulk RNA-seq (Hum et al., 2022). However, differences in the IFN-I signaling have been observed by single-cell RNA seq (Hum et al., 2022), suggesting heterogeneity in the viral RNA sensing and activation of downstream pathways between different cell types.

Finally, we found that *Mavs*$^{-/-}$ mice develop PA and/or Ao vasculitis, characterized by CD11b^{+} and CD3^{+} cell infiltrates upon CHIKV infection. We detected CD3^{+} and CD11b^{+} infiltrates for at least 30 dpi in both Ao and PA. In addition, we found that mice develop focal and multifocal myocarditis in the ventricular region as well as local inflammation in the atria. Intriguingly, the multifocal vasculitis was accentuated around the vessels within the myocardium, suggesting that the main source of damage is vascular. Future work is required to assess the main features of CHIKV-induced heart vessel vasculitis and how vasculitis can predispose to long-term cardiac damage. Determining how CHIKV affects major vessels, and the impact of this infection on long-term cardiovascular function can help to develop strategies to monitor patients with such predisposition in endemic areas. Of note, one mouse from our *Mavs*$^{-/-}$ group showed signs of lethargy at 15 dpi and needed to be euthanized. Cardiac tissue showed substantial tissue damage featured by patchy myocyte dystrophic calcification affecting single myocytes, and focal myocarditis composed by inflammatory infiltrates of CD11b^{+} and CD3^{+} cells **(Figure S7A-C**), with no signs of fibrosis **(Figure S7D).** It is important to note that this represents an isolated event since the majority of the *Mavs*$^{-/-}$ mice used in this study did not succumb to CHIKV. These results are intriguing and demonstrate that persistent infection in cardiac tissue leads to cardiac inflammation and potentially cardiac tissue damage. SNPs in the coding region of the human *MAVS* can result in impaired function (Sharma et al., 2021; Xing et al., 2016). In addition, recent studies suggested a link between age and decreased sensing through *MAVS* (McGuire, 2019), which could be a contributing factor to the observed correlation between age and CHIKV severity (Economopoulou et al., 2009; Traverse et al., 2021). Further work should focus on determining if variability in IFN-I responses among individuals can underlie the differential susceptibilities to CHIKV-induced cardiac complications. The identification of the underlying patient-specific causes of susceptibilities to CHIKV-induced cardiac complications is fundamental to pave the way for the development of preventive and therapeutic clinical interventions.

Altogether, this study provides mechanistic insight into how CHIKV can lead to cardiac damage, underscoring the importance of monitoring cardiac function in patients with CHIKV infections and laying the foundation for the development of new approaches to prevent viral-induced cardiac complications.

Acknowledgments. We would like to thank all members of the Stapleford lab for helpful comments on this manuscript. We thank NYUMC Experimental Pathology Research Laboratory specially Mark Alu and Branka Brukner Dabovic. We are also grateful to the NYU Genome Technology Center for assistance during sequencing and the NYU Langone Microscopy Laboratory for assistance during imaging. We thank Drs. Ken Cadwell and Michael Diamond who kindly provided essential reagents. We are really thankful to Drs. Dominick Papandrea and Ludovic Desvignes for BSL3 assistance. We thank Drs. Ken Cadwell and Victor Torres for critical reading of the manuscript. This work was supported by a start-up package from the NYU Grossman School of Medicine (K.A.S), NIH/NIAID R01 AI162774-01A1 (K.A.S) and 1R01AI143861 (K.M.K), the NYU Cardiovascular Research Center Program pilot grant (K.A.S. and M.G.N), the American Heart Association Postdoctoral Fellowship 19-A0-00-1003686 (M.G.N.), Public Health Service Institutional Research Training Award T32 AI 7180-39 (B.A.R-R.), Training Program in Immunology and Inflammation Training Award 5-T32 AI100853-10 (E.B.). The Experimental Pathology Research Laboratory, the NYU Langone Microscopy Laboratory and the NYU Genome Technology Core are partially supported by NYU Cancer Center support grant P30CA016087 and by NYU Langone's Laura and Isaac Perlmutter Cancer Center.

Author Contributions. M.G.N. and K.A.S. conceived the project and designed experiments; M.G.N, E.B., S.N.S, S.T.Y, P.D.Y, B.A.R.R. performed experiments, F.I. analyzed RNA-seq data; M.G.N, E.B., F.I., and K.A.S. analyzed data, C.L. oversaw histology experiments, N.N. performed histopathology analysis;

V.M. develop the Visiopharm app for histology analysis; M.Z.D. performed slide cryosections; K.K and K.A.S supervised the project. M.G.N. and K.A.S. wrote the original draft, and all authors were involved in manuscript review and editing.

Declaration of Interests.
The authors declare there are no conflicts of interest.

RESOURCE AVAILABILITY

Lead Contact

Further information and requests for resources and reagents should be directed to and will be fulfilled by the Lead Contact, Kenneth Stapleford (Kenneth.stapleford@nyulangone.org)

Material Availability

This study did not generate any unique reagents.

Data and code availability

Bulk RNA sequencing data sets generated in this study are available at GEO: GSE204689. Code is available at GitHub: https://github.com/fizzo13/CHIKV. Any additional information required to reanalyze the data reported in this paper is available from the lead contact upon request.

EXPERIMENTAL MODELS DETAILS

Cells. Cell lines were maintained at 37ºC in 5% CO_2. Baby hamster kidney (BHK-21, ATCC CCL-10) were grown in Dulbecco's modified Eagle's medium (DMEM; Corning) supplemented with 10% fetal bovine serum (FBS; Atlanta Biologicals) and 1% nonessential amino acids (NEAA, Gibco). Vero cells (ATCC CCL-81) were grown in DMEM with 10% newborn calf serum (NBCS; Gibco). All the cell lines were confirmed free of mycoplasma using Lookout Mycoplasma PCR detection kit (Sigma-Aldrich).

Viruses. CHIKV (CHIKV strain 06-049; AM258994) and CHIKV reporter (CHIKV-ZsGreen; CHIKV strain 06-049) infectious clones were generated as previously described (Coffey and Vignuzzi, 2011; Noval et al., 2019).

Mosquitoes. *Aedes (Ae.) albopictus* eggs from Tallman Island Wastewater Treatment Plant in Queens, New York City, were collected by the New York Department of Health (Kaczmarek et al., 2020). Mosquitoes were reared and maintain in Memmert humidified chambers at 28 ºC with 70% humidity and 12 h diurnal light cycle. All the transmission studies were done with mosquitoes in generation F7.

Mice. All mice were housed with food and water ad libitum under 12 h dark/light cycle in a pathogen-free facility at NYU Grossman School of Medicine. Experimental animals were housed in groups of up to 5 mice per cage. Mice were bred and grown in house and maintained in the same facility under specific pathogen-free conditions included the following strains: C57BL/6J wild type mice (000664, Jackson Laboratories). C57BL/6(027) wild type mice (Charles River Laboratories), *Ifnar1*$^{-/-}$ (028288, Jackson Laboratories); *Myd88*$^{-/-}$ (009088, Jackson Laboratories); *Casp1/11*$^{-/-}$ (016621, Jackson Laboratories); *Mavs*$^{-/-}$ (008634, Jackson Laboratories), *Trif*$^{Lps2/Lps2}$ (005037, Jackson Laboratories). *Mxra8*$^{\Delta 8/\Delta 8}$ mice were a gift from Dr. Michael Diamond at Washington University in St. Louis. All mice were bred as heterozygotes to generate WT and KO littermate controls, and subsequent WT or KO colonies coming from littermate controls were used for experiments.

METHODS DETAILS

Biosafety. Work with CHIKV was performed in a biosafety level 3 (BSL-3) laboratory at NYU Grossman School of Medicine.

Virus rescue from infectious clones. Briefly, 10 µg of each of the infection clone plasmids were linearized overnight with NotI (Thermo-Scientific) at 37ºC, phenol:chloroform extracted, ethanol precipitated, and resuspended in nuclease-free water at 1 µg/µl. *In vitro* transcribed viral RNAs were produced using the SP6 mMESSAGE mMACHINE kit (Ambion) following the manufacturer's instructions. After RNA synthesis, samples were DNAse treated, and RNAs were purified by phenol:chloroform extraction, ethanol precipitation, and resuspended in nuclease-free water at a concentration of 1 µg/µl. RNA integrity was confirmed by gel electrophoresis (1% agarose). RNA was aliquoted and stored at -80 ºC until electroporation. Infectious virus was produced by electroporating BHK cells with *in vitro* transcribed viral RNAs. For that purpose, cells were trypsinized, washed twice with ice-cold DPBS (Corning), and resuspended at $1x10^7$ cells/ml in PBS. 390 µl of cells were mixed with 10 µg of *in vitro* transcribed RNA and added to a 2 mm electroporation cuvette (BioRad). BHK-21 cells were electroporated with 1 pulse at 1.2 kV, 25 µF, with infinite resistance. Cells were allowed to recover for 10 min at room temperature (RT), transferred into 6 ml of warm DMEM supplemented with 10% FBS and 1% NEAA, and placed in a T25 flask at 37ºC for 72 h. Virus was harvested, clarified at 1,200 x g for 5 min, and 3 ml of the clarified supernatants were used to infect T175 flask to generate working stocks (Passage 1). Viral titers were determined by plaque assay in Vero cells.

Plaque assay. 10-fold dilutions of each virus in DMEM were added to a monolayer of Vero cells for 1 h at 37ºC. Following incubation, cells were overlaid with 0.8% agarose in DMEM containing 2% NCBS and incubated at 37ºC for 72 h. The cells were fixed with 4% formalin, the agarose plug removed, and plaques visualized by crystal violet staining. Titers were determined by counting plaques on the highest countable dilution. To generate heat-inactivated virus (HI), virus stocks with titers of 10^6 PFU/ml were incubated in a water bath at 56ºC for 4 h. Loss of infectivity was confirmed by plaque assay on Vero cells.

Mosquito infections. *Ae. albopictus* mosquitoes from Tallman (F7) were exposed to an artificial blood meal containing 10^6 PFU/ml CHIKV. Briefly, viruses were mixed 1:2 with PBS-washed sheep blood (Fisher Scientific, MA, USA) supplemented with 5 mM ATP. Mosquitoes exposed to non-infectious blood meals were used as non-infected controls. Female mosquitoes were allowed to feed on 37 ºC blood meals through an artificial membrane for 60 to 90 min. Engorged females were identified, sorted and incubated at 28 ºC with 10% sucrose ad libitum for 7 days. Prior to transmission, mosquitoes were food deprived for 12 h.

Mouse infections. Animal experiments were performed in accordance with all NYU Grossman School of Medicine Institutional Animal Care and Use Committee guidelines (IACUC) and in accordance with guidelines from the National Institutes of Health, the Animal Welfare Act, and the U.S. Federal Law. All mouse studies were performed under BSL-3 conditions. Infections were carried out by either intradermal inoculation, mosquito bite, or intravenous injection via tail vein injections. Briefly, 6-8-week-old male and female were infected with 10^5 PFU of CHIKV, CHIKV-ZsGreen, or mock-infected with carrier (PBS or DMEM) or heat inactivated virus (HI). For intradermal inoculation, mice were anesthetized by inhalation of isoflurane (Henry Schein Animal Health), and injected with 50 µl of virus or control in the left rear footpad. For intravenous inoculation mice were restrained and injected via tail vein injection with 100 to 200 µl of virus or control inoculum using a 29G insulin syringe (Fisher Scientific). For natural transmission, mice were immobilized over a mesh covered pint cup containing 4 to 8 CHIKV-infected or uninfected (blood only) mosquitoes, and mosquitoes were allowed to feed for 40 min. Afterwards, mice were returned to their cages, mosquitoes were killed and homogenized, and viral titers of the infected mosquitoes were determined by plaque assay. Infected experimental mice were euthanized at different timepoints post infection by CO_2 inhalation. Blood was collected by cardiac puncture, and mice were immediately dissected for transcardiac perfusion. Mice were perfused with 30 ml of cold PBS with a 21G to 23G needle. Quality of cardiac perfusion was assessed by confirming full blood removal in liver and kidneys. Then, hearts were extracted and placed in a 12-well plate with 1 ml PBS. Each heart was opened in four chambers and confirmed free of any blood clot. All the mice in this study were perfused with the exception of those used for histopathology and immunostaining. Heart, calf muscle and pancreas were collected in 500 µl of PBS containing one (heart and pancreas) or two (calf muscle) 5 mm stainless steel beads (QIAGEN), homogenized with TissueLyser II (QIAGEN) at 30 1/s for 2 min (heart and pancreas) or 4 min (calf muscle). Debris was removed by centrifugation at 8,000 rpm for 8 min. Blood was collected in 1.5 ml tubes containing 20 ml of 0.5 M EDTA and centrifuged at 8,000 rpm for 8 min. Viral titers were quantified by plaque assay in Vero cells or $TCID_{50}$ in BHK-21 cells.

Median Tissue Culture Infectious Dose ($TCID_{50}$). Briefly for $TCID_{50}$ determination, BHK-21 cells were seeded into 96-well plates (10,000 cells/well). For heart, muscle and pancreas samples the initial dilution corresponds to a dilution 1:5 from the original homogenate, for serum the initial dilution was 1:20. After the first dilution, ten-fold dilutions of tissue homogenates or serum were made in DMEM supplemented with 1% Antibiotic-Antimycotic (Anti-Anti, Invitrogen). Monolayers were infected with 50 µl of the dilutions. After 1 hour, 100 ml of DMEM + 10% FBS + 1% Anti-Anti was added to each well. Cells were incubated at 37 ºC with 5 % CO2 for 96 h. Plates were inspected under the microscope for evidences of cytopathic effect (CPE). Non-infected tissue was used as negative control, and mock treated wells were included in each plate. Positive wells, corresponds to any well showing CHIKV specific CPE. Negative wells, corresponds to any well with no CPE. Following incubation, cells were fixed with 10% formalin, and visualized under the microscope. Each sample was measured in 6 or 7 technical replicates and the calculation was performed using the online $TCID_{50}$ calculator (https://www.klinikum.uni-heidelberg.de).

RNA extractions and RT-qPCR. RNA extractions were performed using TRIzol™ reagent (Invitrogen, 200 µl of clarified tissue homogenate was added to 500 µl of TRIzol™) following the manufacturer's guidelines. Extracted RNA was quantified and diluted to 200 ng/µl. The number of viral genomes/ml for hearts, calf muscle and pancreas were quantified by RT-qPCR using 1 µg of total RNA as template, the Taqman RNA-to-CT One-Step kit (Applied Biosystems™, Beverly, MA, USA) and CHIKV primers to amplify a small region of nsP4 (*CHIKV* forward (fw): 5'-TCACTCCCTGCTGGACTTGATAGA-3'; reverse (rev): 5'-TTGACGAACAGAGTTAGGAACATACC-3') and a probe (5′-(6-carboxyfluorescein)-AGGTACGCGCTTCAAGTTCGGCG-(black-holequencher)-3′). A standard curve was generated for each dataset using *in vitro* transcribed CHIKV RNAs. Viral genomes in serum and levels of *Isg15* in heart homogenates were measured by SYBR Green Master Mix (Thermo) and following manufacturer's instructions. Briefly, cDNA synthesis was performed using the Maxima H minus-strand kit (Thermo Scientific) and random primers. RT-qPCR was performed on QuantStudio 3 qPCR instrument and using the following primers: *CHIKV* (fw: 5'-TCACTCCCTGCTGGACTTGATAGA-3', and rv: 5'-TTGACGAACAGAGTTAGGAACA TACC-3'); *Isg15* (fw: 5'-GGTGTCCGTGACTAACTCCAT-3', and rv: 5'-TGGAAAGGGTAAGA CCGTCCT-3'), and *18S* (fw: 5'-GTAACCCGTTGAACCCCATT-3', and rv: 5'-CCATCCAA TCGGTAGTAGCG-3'). The relative expression of the respective genes to *18S* expression was calculated using the $\Delta\Delta C_T$ method and values were expressed as fold change normalized to mock-infected control.

RNA extractions and RNA-sequencing analysis. For bulk RNA-sequencing C57BL/6 male mice were infected intravenously with 10^5 PFU of CHIKV or HI control, and hearts were perfused with 30 ml of PBS and collected at 2 and 5 dpi. Hearts were collected in 500 µl of TRIzol™ (Invitrogen) with one 5 mm stainless steel bead and processed as described above. RNA was extracted using Zymo direct-zol RNA purification kit (Zymo research, #R2072) according to the manufacturer's instructions. A total of 500 ng per sample was sent to the NYU Genome Technology Center for quality control assessment, automated TruSeq stranded total RNA, with RiboZero Gold library preparation, and Illumina Novaseq6000 sequencing (single pair 100). FASTQ files were aligned to a concatenated file containing the mouse genome (version mm10) and the CHIKV genome (AM258994) through STAR (v2.5.2) in two pass basic mode using the gencode transcript annotation (vM25). Structural and non-structural CHIKV polyprotein coordinates (CHIKVgp1 and CHIKVgp2) were added to the transcriptome annotation, and the transcript count matrix was generated using the summarize overlaps function form the Genomic Alignments (v1.22.1) package. For quantification of structural and non-structural polyproteins RNA abundance, the counts were normalized as counts per million reads (CPM) and statistical comparisons were performed via Wilcoxon rank sum test using the base R (v.3.6.0). Differential gene expression analysis based on negative binomial distribution was performed using DEseq2 (v1.26.0). For pathways enrichment analysis, genes were ranked based on -Log_{10}(FDR) values, assigning a positive or negative value depending on the direction of change. The pathway lists were obtained from the msigdbr (v7.2.1) package (Hallmark, REACTOME or KEGG) and used as input for GSEA pathway enrichment analysis through the fgsea (v1.12.0) R package. Volcano plots were generated using ggplot2 (v3.3.3) and heatmaps were generated using pheatmap (v1.0.12).

Tissue preparation for immunofluorescence and confocal microscopy. Hearts were removed from euthanized mice and fixed in PFA, lysine and periodate buffer (PLP, 0.05 M phosphate buffer, 0.1 M L-lysine, pH 7.4, 2 mg/ml $NaIO_4$, and 10 mg/ml paraformaldehyde) at 4°C for 24 h. Next, tissues were dehydrated in 30% sucrose overnight at 4°C and subsequently embedded in OCT media. Frozen tissue sections were sectioned at 5 µm thickness at the NYU Experimental Pathology Research Laboratory. Fc receptors were blocked with 0.5% anti-CD16/32 Fc block antibody (Biolegend, clone 93) diluted in PBS containing 2% goat serum (Vector Laboratories, S-1000), 2% FBS (Atlanta) and 0.25% Triton-X 100 (Fisher, BP151-100) for 1 h at RT. Sections were washed 5 times with the same buffer, and treated with Trueblack Lipofuscin autofluorescence quencher (Biotium, CAT23007) in ethanol 70% (5% v/v) for 1 min. Sections were washed 5 times and stained with eF570-αSMA (Invitrogen, clone: 1A4) with either APC-CD45 (BioLegends, clone: 30-F11), AF647-TNT (BD Pharmingen, clone: 13-11), AF647-CD31 (BioLegends, clone: MEC13.3) or AF647-Vimentin (Abcam, clone: EPR3776) for 1 h, at RT. All antibodies were used at 1:100 dilution. For IFITM3 staining, slides were stained with 1:100 anti-Fragilis antibody (Abcam, polyclonal) for 1h at RT; washed and stained with a secondary AF555-anti-Rabbit antibody (Invitrogen) at 1:1000 dilution for 1 h. All the slides were then stained with DAPI (Thermo) at 1:1000 dilution. Sections were washed with the same buffer and mount for microscopy analysis. Images were acquired using a Zeiss LSM 880 confocal microscope (Carl Zeiss).

Imaris surface colocalization analysis. The imaging data were processed and analyzed using Imaris software version 9.8 (Bitplane; Oxford Instruments). Briefly, surfaces were built for each channel using specific threshold, number of voxels and surface grain size. The selection of parameters was dependent on each experimental set of images. Once the parameters were defined batch analysis was performed to calculate the total amount of overlapping surfaces between two channels. Analysis was performed on 2x2 tiled images acquired at 20x magnification from the Zeiss 880 confocal microscope, where 2 to 4 different sections per slide were imaged from two to three independent animals per condition.

Histopathology. The heart and part of the aortic arc were removed from euthanized mice, fixed in 10% buffered formalin (Fisher Scientific) for 72 h, and processed through graded ethanol, xylene and into paraffin in a Leica Peloris automated processor. Five-micron paraffin-embedded sections were cut parallel to the long axis of the heart from two to three distinct levels (400 µm, 800 µm, and 1200 µm; or 800 µm, and 1200 µm). Sections of the 4-chamber heart were deparaffinized and stained with hematoxylin and eosin (H&E) on a Leica ST5020 automated histochemical stainer or immunostained on a Leica BondRX® autostainer, according to the manufacturers' instructions. In brief, sections for immunostaining underwent epitope retrieval for 20 min at 100 ºC with Leica Biosystems ER2 solution (pH9, AR9640) followed by a 30 min incubation at 22 ºC with either anti-CD11b (Novus, NB110-89474) diluted 1:10,000, with anti-CD3 (CST, 78588S; clone E4T1B) diluted 1:1,000 or with anti-cleaved CASP3 (CST, 9579S, clone D3E9). The primary antibodies were detected using the BOND Polymer Refine Detection System (Leica, DS9800). Sections were counterstained with hematoxylin scanned on either a Leica AT2 or Hamamatsu Nanozoomer HT whole slide scanners and imported into the NYU Omero image database for viewing and annotation. The severity of tissue pathology and determination of the different categories described in Table S1 and S5, were blindly analyzed by a pathologist (N.N.). Masson trichrome staining was performed as previously described (Carson, 1997). In brief, deparaffinized slides were further fixed in Bouin solution for 1 h at 60 ºC. The slides were then serially

stained with Weigert Hematoxylin (Polysciences, 25088B1&B2) for 10 min, followed by Biebrich Scarlet-Acid Fuchsin (Polysciences, 25088C) for 1 min and Phosphotungstic acid (Polysciences, 25088D) for 10 mins with washes between each step. Slides were then transferred directly into aniline blue (Polysciences, 25088E) for 5 min and differentiated in 1% acetic acid (Polysciewnces, 25088f) for 1 min before dehydration and mounting with permount (Fisher, SP15-100).

CASP3 and CD3 IHC quantification analysis. To determine the number of cleaved $CASP3^+$ or $CD3^+$ cells whole slide scans were analyzed using Visiopharm^R image analysis software version 2021.09. Images were imported to Visiopharm^R's database. Manual outlining of regions of interest (ROI) was performed to divide the four-chamber heart section into right, left ventricles, septum and atria. A Visiopharm^R app was generated to detect DAB-stained cells in the mouse heart. Briefly, image pre-processing steps were run to create features enhancing DAB signal and nuclear signal through color deconvolution and filtering. Segmentation was achieved using a trainable linear bayesian algorithm. Post-processing steps were applied to define nuclei as positive or negative. Results were provided as number of total nuclei, number of positive and number of negative nuclei per ROI analyzed.

Cytokine and chemokine analysis. Mice were infected intravenously with 10^5 PFU of CHIKV or HI control, and heart were collected at 2 and 5 dpi. Heart tissue homogenates generated as described above were diluted 1:5 in 5X PBS:HALT protease inhibitor EDTA-free (Thermo). Total amount of protein was quantified using BCA protein assay (Thermo Fisher Scientific) and samples were diluted to 1.5 mg/ml in PBS:HALT protease inhibitor, 75 ml aliquots were made and stored at -80ºC until needed. Heart homogenates were analyzed for cytokine and chemokine levels using a Bio-Plex Pro Mouse Cytokine 23-plex Assay kit (Bio-Rad, #m60009rdpd) according to the manufacturer's instructions.

Mouse Cardiac troponin-T ELISA. Mice were infected intravenously with 10^5 PFU of CHIKV or HI control, and blood collected as described above, incubated at RT for 30 min, and centrifuged at 1000 x g for 15 min at 4ºC. The upper phased was then transferred to a clean tube and centrifuged at 10,000 x g for 10 minutes. Samples were moved to a clean tube and then 50 ml aliquots were made and stored at -80ºC until needed. Serum was analyzed for mouse cardiac troponin-T using a precoated microtiter plate (amsbio, AMS.E03T0017) according to the manufacturer's instructions.

Single-cell analysis of *Tabula Muris* datasets. Data from *Tabula muris* (Tabula Muris et al., 2018) was downloaded from https://tabula-muris.ds.czbiohub.org. Data was analyzed using the Seurat (v3.2.1) R package. Briefly, data was normalized using the "Normalize Data" function with default parameters. After normalization, we applied the function "Find Variable Features" to identify genes of interest used for downstream dimensionality reduction via the function "RunPCA" and clustering through the "Find Neighbors" and "Find Clusters" functions, with default parameters. The original cluster annotations from *Tabula Muris* were maintained. Violin plots were generated with the "VlnPlot" function. For *Mxr8* and *Fhl1* co-expression, the proportion of cells showing co-expression was calculated based on binarized receptor levels, based on the presence of a minimum of one unique molecular identifier mapping to the gene. Dot plot for normalized expression of potential cell markers was generated using the "DotPlot" function.

QUANTIFICATION AND STATISICAL ANALYSIS

Statistical analysis. Statistical significance was assigned when *P* values were < 0.05 using Prism Version 9 (GraphPad) or R-studio (v3.6.0). Specific tests with exact *P* values are indicated in the Figure legends. All experiments were performed at least in biological duplicates.

Supplementary Tables (Excel Tables)

Table S2. List of differentially expressed genes at 2 dpi (Related to Figure 4).

Table S3. List of differentially expressed genes at 5 dpi (Related to Figure 4).

REFERENCES

Alvarez, M.F., Bolivar-Mejia, A., Rodriguez-Morales, A.J., and Ramirez-Vallejo, E. (2017). Cardiovascular involvement and manifestations of systemic Chikungunya virus infection: A systematic review. F1000Res *6*, 390.

Araiza-Garaygordobil, D., Garcia-Martinez, C.E., Burgos, L.M., Saldarriaga, C., Liblik, K., Mendoza, I., Martinez-Selles, M., Scatularo, C.E., Farina, J.M., Baranchuk, A.*, et al.* (2021). Dengue and the heart. Cardiovasc J Afr *32*, 276-283.

Brauninger, H., Stoffers, B., Fitzek, A.D.E., Meissner, K., Aleshcheva, G., Schweizer, M., Weimann, J., Rotter, B., Warnke, S., Edler, C.*, et al.* (2022). Cardiac SARS-CoV-2 infection is associated with pro-inflammatory transcriptomic alterations within the heart. Cardiovasc Res *118*, 542-555.

Camelliti, P., Borg, T.K., and Kohl, P. (2005). Structural and functional characterisation of cardiac fibroblasts. Cardiovasc Res *65*, 40-51.

Carson, F.L. (1997). Histotechnology: A Self-Instructional Text, 2nd Ed edn (ASCP Press).

Chen, W., Foo, S.S., Zaid, A., Teng, T.S., Herrero, L.J., Wolf, S., Tharmarajah, K., Vu, L.D., van Vreden, C., Taylor, A.*, et al.* (2017). Specific inhibition of NLRP3 in chikungunya disease reveals a role for inflammasomes in alphavirus-induced inflammation. Nat Microbiol *2*, 1435-1445.

Ciancanelli, M.J., Huang, S.X., Luthra, P., Garner, H., Itan, Y., Volpi, S., Lafaille, F.G., Trouillet, C., Schmolke, M., Albrecht, R.A.*, et al.* (2015). Infectious disease. Life-threatening influenza and impaired

interferon amplification in human IRF7 deficiency. Science *348*, 448-453.
Clavarino, G., Claudio, N., Couderc, T., Dalet, A., Judith, D., Camosseto, V., Schmidt, E.K., Wenger, T., Lecuit, M., Gatti, E.*, et al.* (2012). Induction of GADD34 is necessary for dsRNA-dependent interferon-beta production and participates in the control of Chikungunya virus infection. PLoS Pathog *8*, e1002708.
Coffey, L.L., and Vignuzzi, M. (2011). Host alternation of chikungunya virus increases fitness while restricting population diversity and adaptability to novel selective pressures. J Virol *85*, 1025-1035.
Cotella, J.I., Farina, J.M., and Noval, M.G. (2021). Chikungunya and Heart. In Neglected Tropical Diseases and other Infectious Diseases affecting the Heart, A.B. Clara Saldarriaga, ed. (Elselvier).
Crosby, L., Perreau, C., Madeux, B., Cossic, J., Armand, C., Herrmann-Storke, C., Najioullah, F., Valentino, R., and Thiery, G. (2016). Severe manifestations of chikungunya virus in critically ill patients during the 2013-2014 Caribbean outbreak. Int J Infect Dis *48*, 78-80.
de Lima, S.T.S., de Souza, W.M., Cavalcante, J.W., da Silva Candido, D., Fumagalli, M.J., Carrera, J.P., Simoes Mello, L.M., De Carvalho Araujo, F.M., Cavalcante Ramalho, I.L., de Almeida Barreto, F.K.*, et al.* (2021). Fatal Outcome of Chikungunya Virus Infection in Brazil. Clin Infect Dis *73*, e2436-e2443.
Diamond, M.S., and Farzan, M. (2013). The broad-spectrum antiviral functions of IFIT and IFITM proteins. Nat Rev Immunol *13*, 46-57.
Economopoulou, A., Dominguez, M., Helynck, B., Sissoko, D., Wichmann, O., Quenel, P., Germonneau, P., and Quatresous, I. (2009). Atypical Chikungunya virus infections: clinical manifestations, mortality and risk factors for severe disease during the 2005-2006 outbreak on Reunion. Epidemiol Infect *137*, 534-541.
Ekchariyawat, P., Hamel, R., Bernard, E., Wichit, S., Surasombatpattana, P., Talignani, L., Thomas, F., Choumet, V., Yssel, H., Despres, P.*, et al.* (2015). Inflammasome signaling pathways exert antiviral effect against Chikungunya virus in human dermal fibroblasts. Infect Genet Evol *32*, 401-408.
Fan, J., Ye, J., Kamphorst, J.J., Shlomi, T., Thompson, C.B., and Rabinowitz, J.D. (2014). Quantitative flux analysis reveals folate-dependent NADPH production. Nature *510*, 298-302.
Farias, L., Beserra, F., Fernandes, L., Teixeira, A.A.R., Ferragut, J.M., Girao, E.S., and Pires Neto, R.D.J. (2019). Myocarditis Following Recent Chikungunya and Dengue Virus Coinfection: A Case Report. Arq Bras Cardiol *113*, 783-786.
Fox, J.M., and Diamond, M.S. (2016). Immune-Mediated Protection and Pathogenesis of Chikungunya Virus. J Immunol *197*, 4210-4218.
Gasque, P., Bandjee, M.C., Reyes, M.M., and Viasus, D. (2016). Chikungunya Pathogenesis: From the Clinics to the Bench. J Infect Dis *214*, S446-S448.
Gorbea, C., Makar, K.A., Pauschinger, M., Pratt, G., Bersola, J.L., Varela, J., David, R.M., Banks, L., Huang, C.H., Li, H.*, et al.* (2010). A role for Toll-like receptor 3 variants in host susceptibility to enteroviral myocarditis and dilated cardiomyopathy. J Biol Chem *285*, 23208-23223.
Hsu, C.H., Cruz-Lopez, F., Vargas Torres, D., Perez-Padilla, J., Lorenzi, O.D., Rivera, A., Staples, J.E., Lugo, E., Munoz-Jordan, J., Fischer, M.*, et al.* (2019). Risk factors for hospitalization of patients with chikungunya virus infection at sentinel hospitals in Puerto Rico. PLoS Negl Trop Dis *13*, e0007084.
Hum, N.R., Bourguet, F.A., Sebastian, A., Lam, D., Phillips, A.M., Sanchez, K.R., Rasley, A., Loots, G.G., and Weilhammer, D.R. (2022). MAVS mediates a protective immune response in the brain to Rift Valley fever virus. PLoS Pathog *18*, e1010231.
Ivey, M.J., and Tallquist, M.D. (2016). Defining the Cardiac Fibroblast. Circ J *80*, 2269-2276.
Kaczmarek, M.E., Herzog, N.L., Noval, M.G., Zuzworsky, J., Shah, Z., Bajwa, W.I., and Stapleford, K.A. (2020). Distinct New York City Aedes albopictus Mosquito Populations Display Differences in Salivary Gland Protein D7 Diversity and Chikungunya Virus Replication. Viruses *12*.
Kenney, A.D., McMichael, T.M., Imas, A., Chesarino, N.M., Zhang, L., Dorn, L.E., Wu, Q., Alfaour, O., Amari, F., Chen, M.*, et al.* (2019). IFITM3 protects the heart during influenza virus infection. Proc Natl Acad Sci U S A *116*, 18607-18612.
Lane, E.B., Hogan, B.L., Kurkinen, M., and Garrels, J.I. (1983). Co-expression of vimentin and cytokeratins in parietal endoderm cells of early mouse embryo. Nature *303*, 701-704.
Langsjoen, R.M., Zhou, Y., Holcomb, R.J., and Routh, A.L. (2021). Chikungunya Virus Infects the Heart and Induces Heart-Specific Transcriptional Changes in an Immunodeficient Mouse Model of Infection. Am J Trop Med Hyg *106*, 99-104.
Lasrado, N., Borcherding, N., Arumugam, R., Starr, T.K., and Reddy, J. (2022). Dissecting the cellular landscape and transcriptome network in viral myocarditis by single-cell RNA sequencing. iScience *25*, 103865.
Lemant, J., Boisson, V., Winer, A., Thibault, L., Andre, H., Tixier, F., Lemercier, M., Antok, E., Cresta, M.P., Grivard, P.*, et al.* (2008). Serious acute chikungunya virus infection requiring intensive care during the Reunion Island outbreak in 2005-2006. Crit Care Med *36*, 2536-2541.
Li, Z., Nguyen, T.T., and Valaperti, A. (2021). Human cardiac fibroblasts produce pro-inflammatory cytokines upon TLRs and RLRs stimulation. Mol Cell Biochem *476*, 3241-3252.
Long, K.M., and Heise, M.T. (2015). Protective and Pathogenic Responses to Chikungunya Virus Infection. Curr Trop Med Rep *2*, 13-21.
McGuire, P.J. (2019). Mitochondrial Dysfunction and the Aging Immune System. Biology (Basel) *8*.
Meertens, L., Hafirassou, M.L., Couderc, T., Bonnet-Madin, L., Kril, V., Kummerer, B.M., Labeau, A., Brugier, A., Simon-Loriere, E., Burlaud-Gaillard, J.*, et al.* (2021). FHL1 is a key player of chikungunya virus tropism and pathogenesis. C R Biol *343*, 79-89.

Minhas, A.M., Nayab, A., Iyer, S., Narmeen, M., Fatima, K., Khan, M.S., and Constantin, J. (2017). Association of Zika Virus with Myocarditis, Heart Failure, and Arrhythmias: A Literature Review. Cureus *9*, e1399.
Noval, M.G., Rodriguez-Rodriguez, B.A., Rangel, M.V., and Stapleford, K.A. (2019). Evolution-Driven Attenuation of Alphaviruses Highlights Key Glycoprotein Determinants Regulating Viral Infectivity and Dissemination. Cell Rep *28*, 460-471 e465.
Planavila, A., Redondo-Angulo, I., Ribas, F., Garrabou, G., Casademont, J., Giralt, M., and Villarroya, F. (2015). Fibroblast growth factor 21 protects the heart from oxidative stress. Cardiovasc Res *106*, 19-31.
Poddar, S., Hyde, J.L., Gorman, M.J., Farzan, M., and Diamond, M.S. (2016). The Interferon-Stimulated Gene IFITM3 Restricts Infection and Pathogenesis of Arthritogenic and Encephalitic Alphaviruses. J Virol *90*, 8780-8794.
Samra, J.A., Hagood, N.L., Summer, A., Medina, M.T., and Holden, K.R. (2017). Clinical Features and Neurologic Complications of Children Hospitalized With Chikungunya Virus in Honduras. J Child Neurol *32*, 712-716.
Scatularo, C.E., Ballesteros, O.A., Saldarriaga, C., Mendoza, I., Wyss, F., Liprandi, A.S., Munera, A., Liendro, M.C., Baranchuk, A., Neglected Tropical, D.*, et al.* (2022). Zika & heart: A systematic review. Trends Cardiovasc Med *32*, 52-58.
Schilte, C., Buckwalter, M.R., Laird, M.E., Diamond, M.S., Schwartz, O., and Albert, M.L. (2012). Cutting edge: independent roles for IRF-3 and IRF-7 in hematopoietic and nonhematopoietic cells during host response to Chikungunya infection. J Immunol *188*, 2967-2971.
Schilte, C., Couderc, T., Chretien, F., Sourisseau, M., Gangneux, N., Guivel-Benhassine, F., Kraxner, A., Tschopp, J., Higgs, S., Michault, A.*, et al.* (2010). Type I IFN controls chikungunya virus via its action on nonhematopoietic cells. J Exp Med *207*, 429-442.
Sharma, A., Kontodimas, K., and Bosmann, M. (2021). The MAVS Immune Recognition Pathway in Viral Infection and Sepsis. Antioxid Redox Signal *35*, 1376-1392.
Sharp, T.M., Keating, M.K., Shieh, W.J., Bhatnagar, J., Bollweg, B.C., Levine, R., Blau, D.M., Torres, J.V., Rivera, A., Perez-Padilla, J.*, et al.* (2021). Clinical Characteristics, Histopathology, and Tissue Immunolocalization of Chikungunya Virus Antigen in Fatal Cases. Clin Infect Dis *73*, e345-e354.
Tabula Muris, C., Overall, c., Logistical, c., Organ, c., processing, Library, p., sequencing, Computational data, a., Cell type, a., Writing, g.*, et al.* (2018). Single-cell transcriptomics of 20 mouse organs creates a Tabula Muris. Nature *562*, 367-372.
Tarbit, E., Singh, I., Peart, J.N., and Rose'Meyer, R.B. (2019). Biomarkers for the identification of cardiac fibroblast and myofibroblast cells. Heart Fail Rev *24*, 1-15.
Traverse, E.M., Hopkins, H.K., Vaidhyanathan, V., and Barr, K.L. (2021). Cardiomyopathy and Death Following Chikungunya Infection: An Increasingly Common Outcome. Trop Med Infect Dis *6*.
Tsukamoto, K., Mani, D.R., Shi, J., Zhang, S., Haagensen, D.E., Otsuka, F., Guan, J., Smith, J.D., Weng, W., Liao, R.*, et al.* (2013). Identification of apolipoprotein D as a cardioprotective gene using a mouse model of lethal atherosclerotic coronary artery disease. Proc Natl Acad Sci U S A *110*, 17023-17028.
Villamil-Gomez, W.E., Ramirez-Vallejo, E., Cardona-Ospina, J.A., Silvera, L.A., and Rodriguez-Morales, A.J. (2016). Electrocardiographic alterations in patients with chikungunya fever from Sucre, Colombia: A 42-case series. Travel Med Infect Dis *14*, 510-512.
Wang, Y.T., Lim, Y., McCall, M.N., Huang, K.T., Haynes, C.M., Nehrke, K., and Brookes, P.S. (2019). Cardioprotection by the mitochondrial unfolded protein response requires ATF5. Am J Physiol Heart Circ Physiol *317*, H472-H478.
Werneke, S.W., Schilte, C., Rohatgi, A., Monte, K.J., Michault, A., Arenzana-Seisdedos, F., Vanlandingham, D.L., Higgs, S., Fontanet, A., Albert, M.L.*, et al.* (2011). ISG15 is critical in the control of Chikungunya virus infection independent of UbE1L mediated conjugation. PLoS Pathog *7*, e1002322.
Wilson, J.A., Prow, N.A., Schroder, W.A., Ellis, J.J., Cumming, H.E., Gearing, L.J., Poo, Y.S., Taylor, A., Hertzog, P.J., Di Giallonardo, F.*, et al.* (2017). RNA-Seq analysis of chikungunya virus infection and identification of granzyme A as a major promoter of arthritic inflammation. PLoS Pathog *13*, e1006155.
Xing, F., Matsumiya, T., Hayakari, R., Yoshida, H., Kawaguchi, S., Takahashi, I., Nakaji, S., and Imaizumi, T. (2016). Alteration of Antiviral Signalling by Single Nucleotide Polymorphisms (SNPs) of Mitochondrial Antiviral Signalling Protein (MAVS). PLoS One *11*, e0151173.
Zhang, Q., Bastard, P., Liu, Z., Le Pen, J., Moncada-Velez, M., Chen, J., Ogishi, M., Sabli, I.K.D., Hodeib, S., Korol, C.*, et al.* (2020). Inborn errors of type I IFN immunity in patients with life-threatening COVID-19. Science *370*.
Zhang, R., Earnest, J.T., Kim, A.S., Winkler, E.S., Desai, P., Adams, L.J., Hu, G., Bullock, C., Gold, B., Cherry, S.*, et al.* (2019). Expression of the Mxra8 Receptor Promotes Alphavirus Infection and Pathogenesis in Mice and Drosophila. Cell Rep *28*, 2647-2658 e2645.
Zhang, R., Kim, A.S., Fox, J.M., Nair, S., Basore, K., Klimstra, W.B., Rimkunas, R., Fong, R.H., Lin, H., Poddar, S.*, et al.* (2018). Mxra8 is a receptor for multiple arthritogenic alphaviruses. Nature *557*, 570-574.

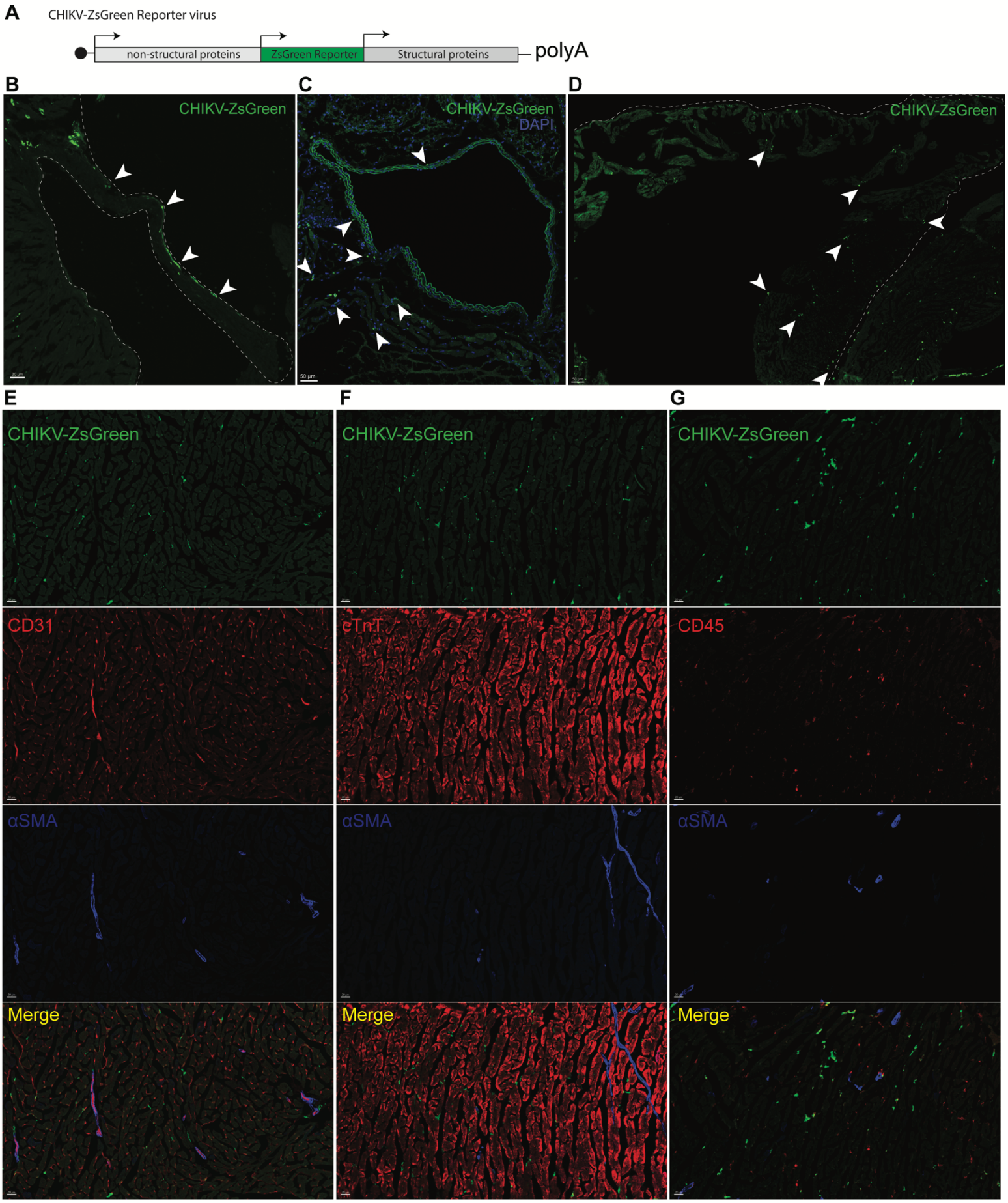
A
CHIKV-ZsGreen Reporter virus
non-structural proteins
ZsGreen Reporter
Structural proteins
polyA
B
CHIKV-ZsGreen
C
CHIKV-ZsGreen
DAPI
D
CHIKV-ZsGreen
E
F
G
CHIKV-ZsGreen
CD31
cTnT
CD45
αSMA
Merge

Figure S1 (Related to Figure 1 and 2). A. Schematic representation of the CHIKV-ZsGreen reporter virus. **B-D.** Examples of infected valves (**B**), vessel (**C**) or atrium (**D**). Green channel: CHIKV infected cells. Gray channel: DAPI. White arrows: CHIKV infected cells. Scale = 30 μm (**B**). Scale= 50 μm (**C-D**). **E-G.** Representative immunofluorescence images of ventricular sections of CHIKV infected WT hearts. The panels represent the individual and merge channels for the different cellular markers: cardiac endothelial cells **(E)**, cardiomyocytes **(F)**, or cardiac leukocytes **(G)**. Scale = 20 μm.

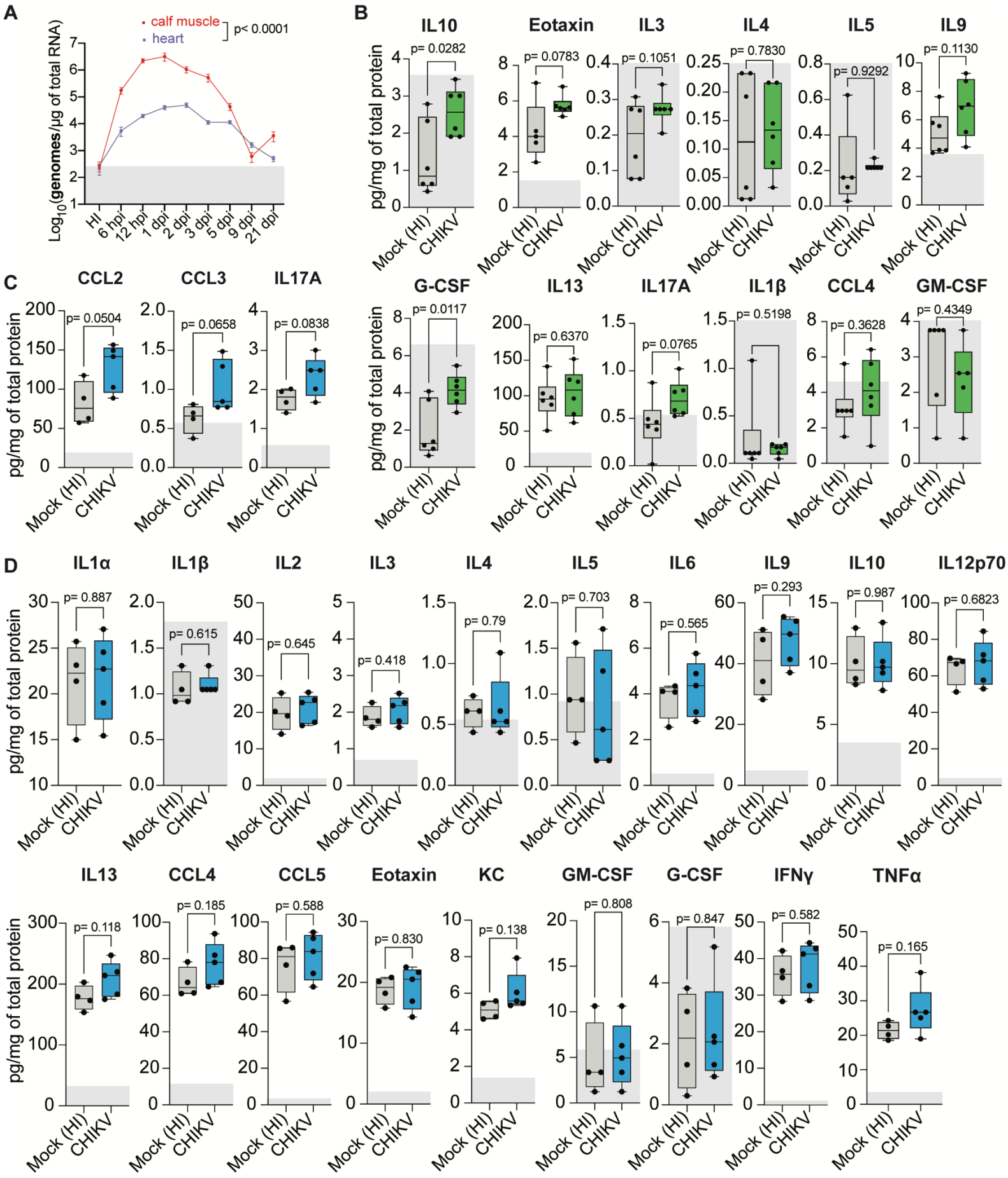
A
calf muscle
heart
p< 0.0001
Log10(genomes/µg of total RNA)
HI
6 hpi
12 hpi
1 dpi
2 dpi
3 dpi
5 dpi
9 dpi
21 dpi
B
IL10
Eotaxin
IL3
IL4
IL5
IL9
p= 0.0282
p= 0.0783
p= 0.1051
p= 0.7830
p= 0.9292
p= 0.1130
C
CCL2
CCL3
IL17A
G-CSF
IL13
IL17A
IL1β
CCL4
GM-CSF
p= 0.0504
p= 0.0658
p= 0.0838
p= 0.0117
p= 0.6370
p= 0.0765
p= 0.5198
p= 0.3628
p= 0.4349
D
IL1α
IL1β
IL2
IL3
IL4
IL5
IL6
IL9
IL10
IL12p70
p= 0.887
p= 0.615
p= 0.645
p= 0.418
p= 0.79
p= 0.703
p= 0.565
p= 0.293
p= 0.987
p= 0.6823
IL13
CCL4
CCL5
Eotaxin
KC
GM-CSF
G-CSF
IFNγ
TNFα
p= 0.118
p= 0.185
p= 0.588
p= 0.830
p= 0.138
p= 0.808
p= 0.847
p= 0.582
p= 0.165
pg/mg of total protein
Mock (HI)
CHIKV

Figure S2 (Related to Figure 3). A. CHIKV replication kinetics in the heart (blue) and the calf muscle (red). Each time point represents the average and the standard deviation of the mean measured for 5 to 10 mice per group. **B-D**. Protein levels of proinflammatory cytokines and chemokines in cardiac tissue homogenates at 2 dpi **(B)** and 5 dpi **(C and D)**. The bottom gray box represents the detection limit for each protein determined as the last value in the calibration curve. N=5 to 6 mice per group. P values were calculated using Mixed-effects model test **(A)** or using Mann Whitney test **(B-D)**.

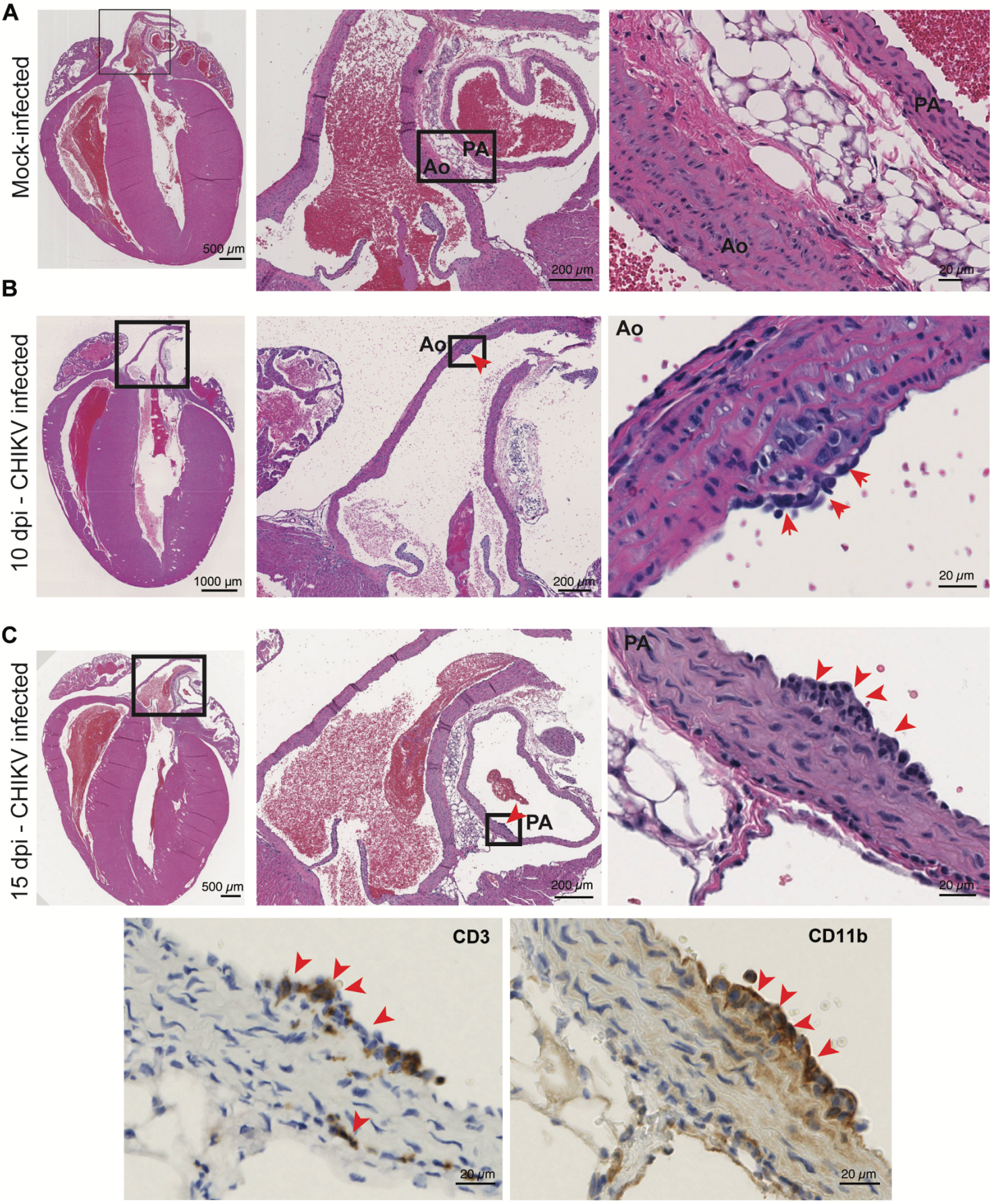
A
Mock-infected
500 µm
PA
Ao
200 µm
PA
Ao
20 µm
B
10 dpi - CHIKV infected
1000 µm
Ao
200 µm
Ao
20 µm
C
15 dpi - CHIKV infected
500 µm
PA
200 µm
PA
20 µm
CD3
20 µm
CD11b
20 µm

Figure S3 (Related to Figure 3 and Table S1). H&E sections showing four-chamber view representation for mock-infected **(A)** or CHIKV-infected WT mice at 10 dpi **(B)** or 15 dpi **(C)** (scale = 1000 μm). The square indicates the aorta and the pulmonary artery (scale= 200 μm), and the right panel shows a zoom in of the indicated area of the aorta **(B)** or the pulmonary artery **(C)** with mononuclear cell infiltrates indicative of endothelialitis (scale= 20 μm). The bottom panel shows CD3 and CD11b staining from consecutive sections for the 15 dpi CHIKV infected mice **(C)**. Red arrows indicate mononuclear cell infiltrates.

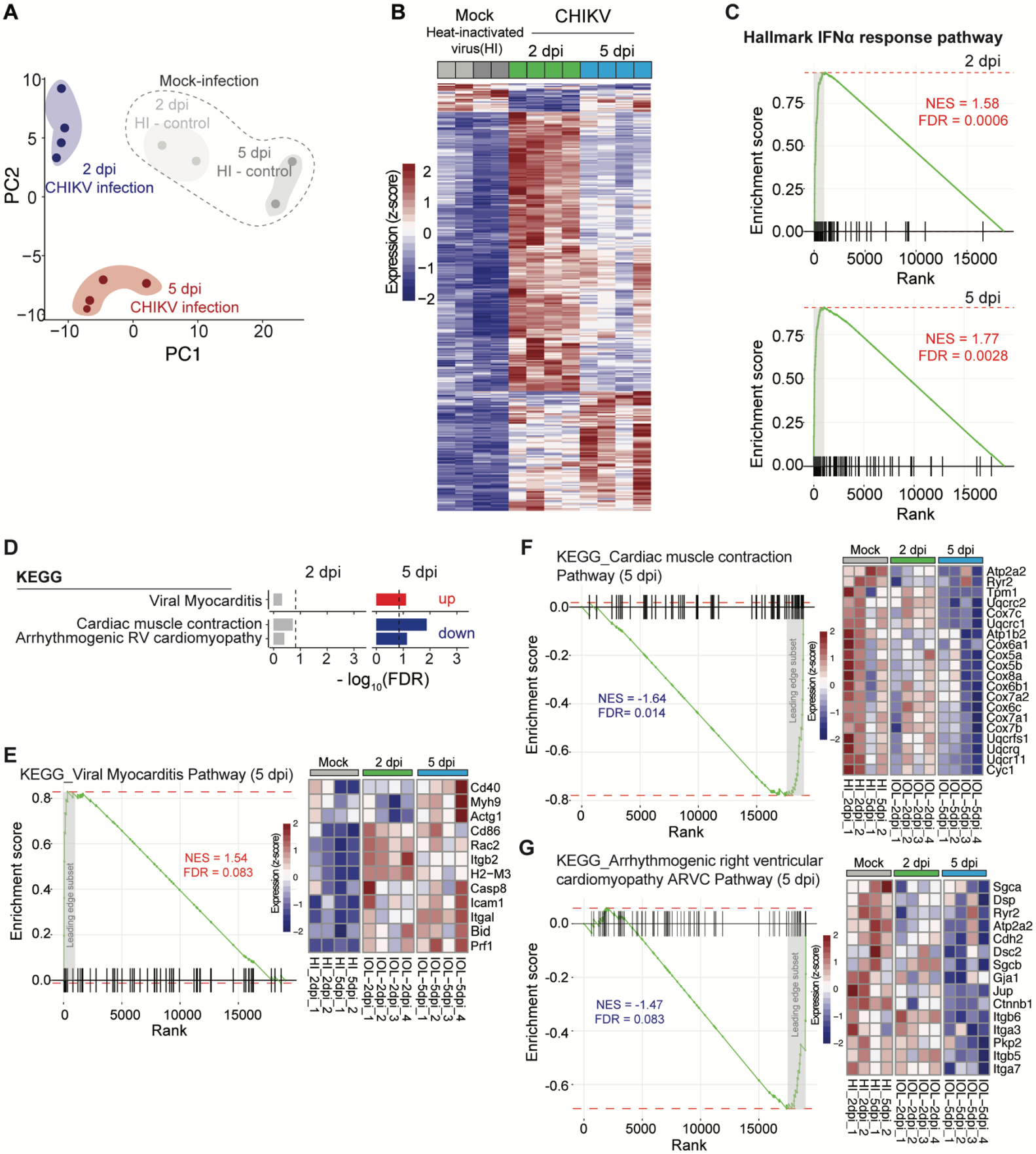
A
Mock-infection
2 dpi
HI - control
5 dpi
HI - control
2 dpi
CHIKV infection
5 dpi
CHIKV infection
PC2
PC1
B
Mock
Heat-inactivated virus(HI)
CHIKV
2 dpi
5 dpi
Expression (z-score)
C
Hallmark IFNα response pathway
2 dpi
NES = 1.58
FDR = 0.0006
5 dpi
NES = 1.77
FDR = 0.0028
Enrichment score
Rank
D
KEGG
2 dpi
5 dpi
Viral Myocarditis
Cardiac muscle contraction
Arrhythmogenic RV cardiomyopathy
up
down
- log10(FDR)
E
KEGG_Viral Myocarditis Pathway (5 dpi)
NES = 1.54
FDR = 0.083
Leading edge subset
Mock
2 dpi
5 dpi
Cd40
Myh9
Actg1
Cd86
Rac2
Itgb2
H2−M3
Casp8
Icam1
Itgal
Bid
Prf1
F
KEGG_Cardiac muscle contraction Pathway (5 dpi)
NES = -1.64
FDR= 0.014
Atp2a2
Ryr2
Tpm1
Uqcrc2
Cox7c
Uqcrc1
Atp1b2
Cox6a1
Cox5a
Cox5b
Cox8a
Cox6b1
Cox7a2
Cox6c
Cox7a1
Cox7b
Uqcrfs1
Uqcrq
Uqcr11
Cyc1
G
KEGG_Arrhythmogenic right ventricular cardiomyopathy ARVC Pathway (5 dpi)
NES = -1.47
FDR = 0.083
Sgca
Dsp
Ryr2
Atp2a2
Cdh2
Dsc2
Sgcb
Gja1
Jup
Ctnnb1
Itgb6
Itga3
Pkp2
Itgb5
Itga7

Figure S4. (Related to Figure 4). A. Principal component analysis (PCA) showing that biological replicates grouped by treatment. **B.** Heatmap showing the differentially expressed genes (FDR < 0.15 and absolute $log_2FC > 1$). The boxes on top indicate the biological replicates for mock (heat-inactivated virus; N = 4; grey boxes) and CHIKV-infected at either 2 dpi (N = 4; green boxes) or 5 dpi (N = 4; blue boxes). **C**. Enrichment plot for the interferon alpha response pathway (Hallmark) at 2 dpi (upper panel) and 5 dpi (bottom panel). **D**. Pathway enrichment analysis of either 2 dpi or 5 dpi. Bars indicate the -log10(FDR); downregulated processes (FDR < 0.15 and NES < 0) are highlighted in blue; upregulated processes (FDR < 0.15 and N > 0) are highlighted in red. **E**. Enrichment plot for the viral myocarditis pathway (KEGG) at 5 dpi (left panel) and heatmaps indicating expression of the leading-edge genes in mock (N = 4) or CHIKV-infected mice at 2 dpi (N = 4) or 5 dpi (N = 4; right panel). **F**. Enrichment plot for the cardiac muscle contraction (KEGG) at 5 dpi (left panel) and heatmaps indicating expression of the leading-edge genes in mock (N = 4) or CHIKV-infected mice at 2 dpi (N =4) or 5 dpi (N = 4; right panel). **G**. Enrichment plot for the viral Arrhythmogenic right ventricular cardiomyopathy (KEGG) at 5 dpi (left panel) and heatmaps indicating expression of the leading-edge genes in mock (N = 4) or CHIKV-infected mice at 2 dpi (N =4) or 5 dpi (N = 4; right panel). NES = normalized enrichment score; grey shadowing indicates the genes belonging to the leading edge.

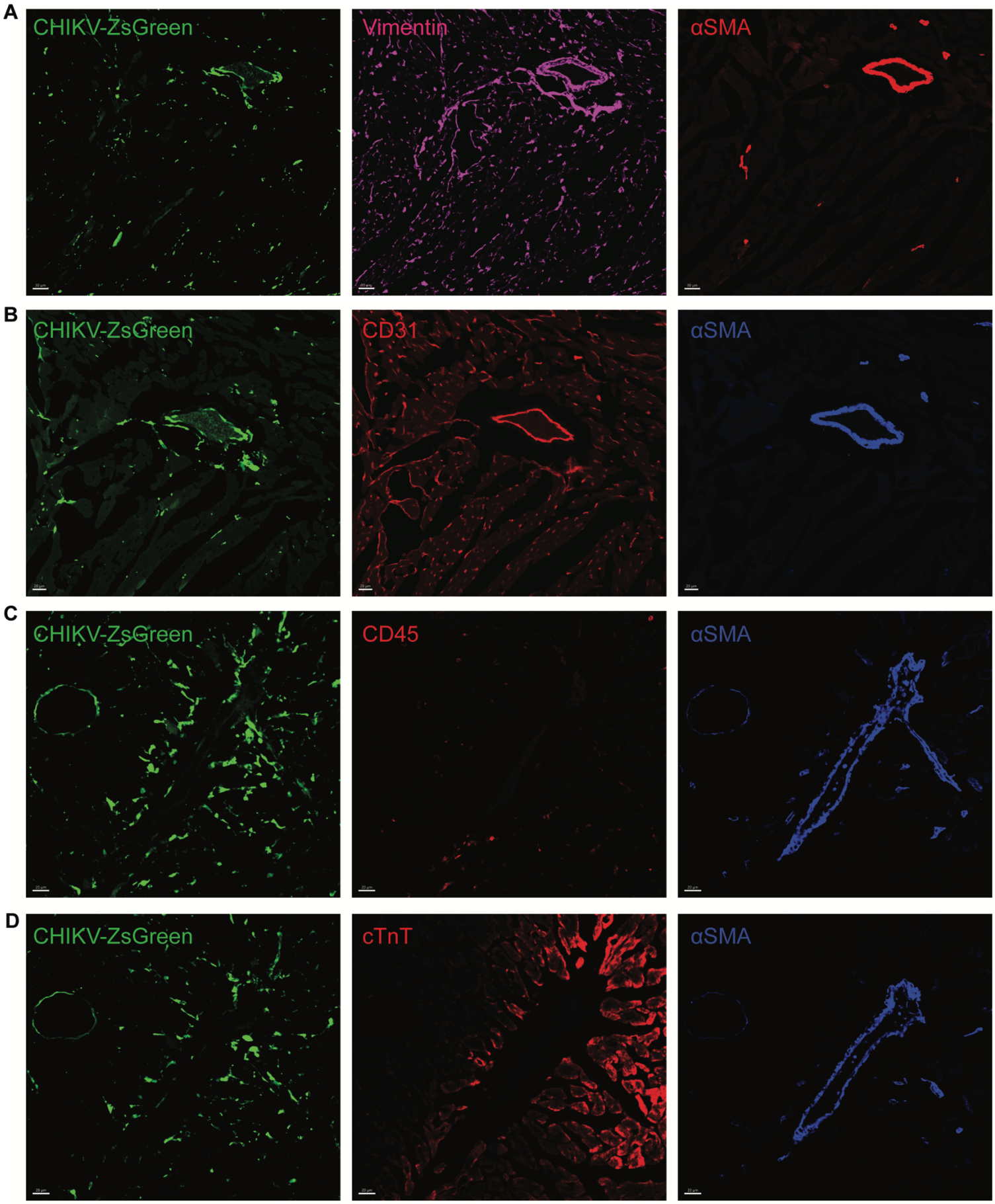
A
CHIKV-ZsGreen
Vimentin
αSMA
B
CHIKV-ZsGreen
CD31
αSMA
C
CHIKV-ZsGreen
CD45
αSMA
D
CHIKV-ZsGreen
cTnT
αSMA

Figure S5. (Related to Figure 5). Representative immunofluorescence images of ventricular sections of CHIKV infected *Ifnar1*$^{-/-}$ hearts. The panels represent the individual channels for the CHIKV-ZsGreen (green channel) and for the different cellular markers used to identified: cardiac fibroblasts **(A)**, cardiac endothelial cells **(B)**, cardiac leukocytes **(C),** and cardiomyocytes **(D)**. Scale = 20 μm.

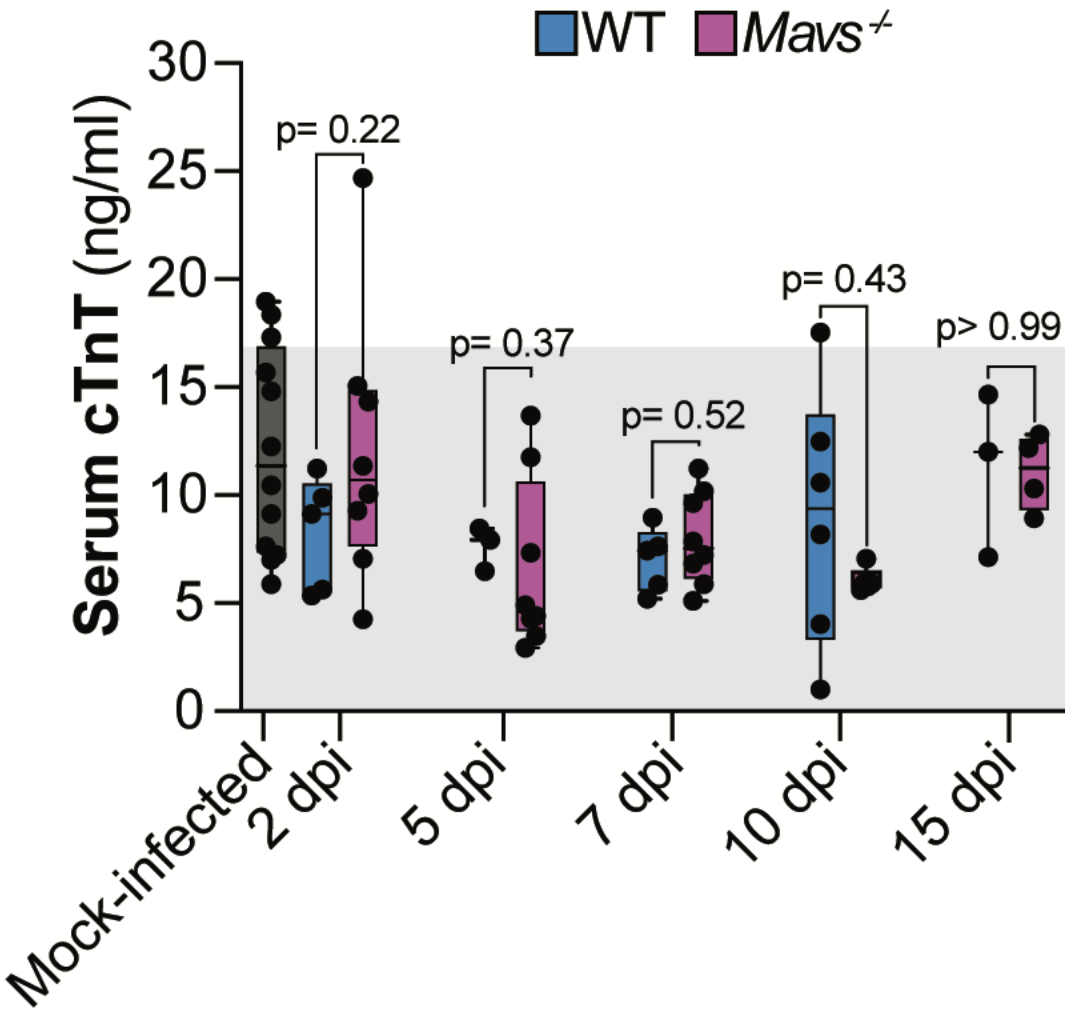

Figure S6. (Related to Figure 7). Serum levels of cardiac troponin-T measured by ELISA. P values were calculated using multiple Mann-Whitney test. Gray box represent the background level corresponding to the mock-infected mice.

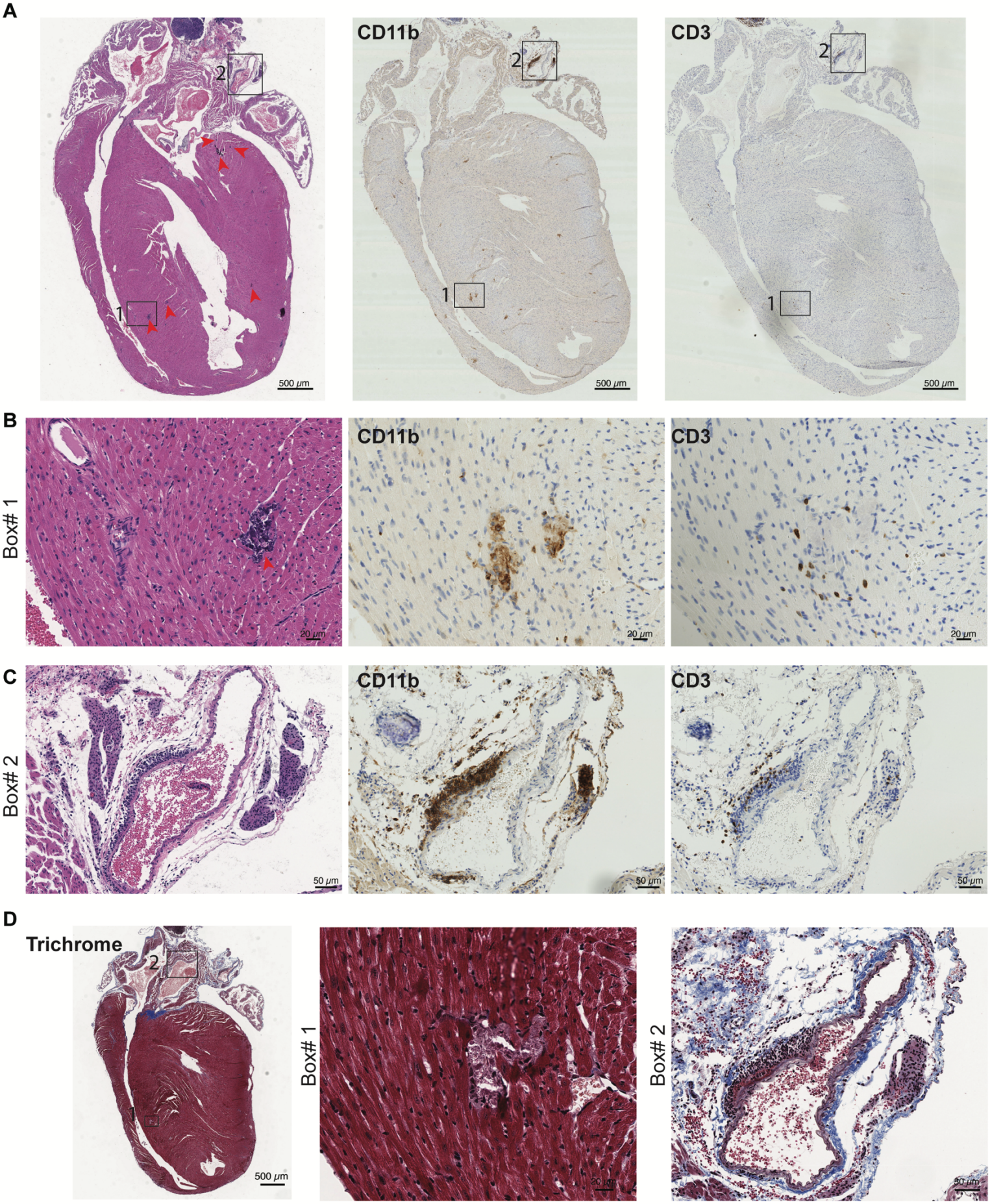
A
CD11b
CD3
1
2
500 µm
B
Box# 1
20 µm
C
Box# 2
50 µm
D
Trichrome
Box# 1
Box# 2

Figure S7. (Related to Figure 7). A. Four-chamber view representation of cardiac tissue from a 15 dpi *Mavs*$^{-/-}$ mouse that succumb to CHIKV infection. Left panel, H&E showing four-chamber view and major vessels at the base of the heart. Middle panel: consecutive section stained with CD11b antibody. Right panel: consecutive section stained with CD3 antibody. Scale = 500 µm. **B.** Magnification of the ventricular region section (Box #1) for H&E, CD11b and CD3 staining showing infiltrates. Scale = 20 µm. **C.** Mason Trichrome staining, showing no signs of fibrosis. **D.** Magnification of the PA section (Box #2) for H&E, CD11b and CD3 staining. Scale = 50 µm. Arrows indicate mononuclear cell infiltrates.

Table S1. Histopathological assessment of H&E sections for WT infected mice (Related to Figure 3, Figure 7 and Figure S3)

Mouse ID	Genotype	Dpi (days)	Condition	Vasculitis			Other Findings
				Vasculitis	Ao	PA	
M1	WT	Mock-infected	DMEM	NO	no	no	
M2	WT	Mock-infected	DMEM	NO	no	no	
M3	WT	Mock-infected	HI control	NO	no	no	
M4	WT	Mock-infected	HI control	NO	no	no	
M5	WT	3 dpi	CHIKV	NO	no	no	
M6	WT	3 dpi	CHIKV	NO	no	no	
M7	WT	3 dpi	CHIKV	NO	no	no	
M8	WT	3 dpi	CHIKV	NA*	na	na	
M9	WT	5 dpi	CHIKV	NO	no	no	
M10	WT	5 dpi	CHIKV	NO	no	no	
M11	WT	5 dpi	CHIKV	NO	no	no	
M12	WT	10 dpi	CHIKV	NO	no	na	
M13	WT	10 dpi	CHIKV	YES**	Yes	no	**Vasculitis (focal endothelialitis in aorta) **(Figure S3B)**
M14	WT	10 dpi	CHIKV	NO	no	na	
M15	WT	15 dpi	CHIKV	NO	no	no	
M16	WT	15 dpi	CHIKV	NO	no	na	
M17	WT	15 dpi	CHIKV	NA*	na	na	
M18	WT	15 dpi	CHIKV	NO	no	no	
M19	WT	15 dpi	CHIKV	YES**	no	Yes	**Vasculitis (focal endothelialitis in PA) **(Figure S3C)**
M20	WT	15 dpi	CHIKV	NO	no	no	
M21	WT	30 dpi	CHIKV	NO	no	no	
M22	WT	30 dpi	CHIKV	NA*	na	na	
M23	WT	30 dpi	CHIKV	NA*	na	na	

NA*: no major vessel in slide; na: no Ao or PA section in that slide; Ao: aorta; PA: pulmonary artery

Table S4, related with Figure 4. Pathway enrichment analysis. Significant regulated HALLMARK pathways. (FDR < 0.15 and normalized enrichment score [NES] > 0). All pathways represented in Figure 3C are highlighted in bold.

	2 dpi	pval	padj	-log10(padj)	NES
1	**HALLMARK_INTERFERON_GAMMA_RESPONSE**	**0.00001**	**0.0005**	**3.30**	**1.62**
2	**HALLMARK_INTERFERON_ALPHA_RESPONSE**	**0.00002**	**0.0006**	**3.22**	**1.58**
3	HALLMARK_ALLOGRAFT_REJECTION	0.00038	0.0063	2.20	1.5
4	**HALLMARK_COMPLEMENT**	**0.003**	**0.032**	**1.49**	**1.44**
5	**HALLMARK_MTORC1_SIGNALING**	**0.003**	**0.032**	**1.49**	**1.44**
6	HALLMARK_KRAS_SIGNALING_UP	0.006	0.054	1.27	1.42
7	**HALLMARK_UNFOLDED_PROTEIN_RESPONSE**	**0.012**	**0.086**	**1.07**	**1.42**
8	**HALLMARK_INFLAMMATORY_RESPONSE**	**0.017**	**0.105**	**0.98**	**1.37**
9	HALLMARK_COAGULATION	0.019	0.108	0.97	1.39
10	HALLMARK_IL6_JAK_STAT3_SIGNALING	0.022	0.112	0.95	1.4
11	HALLMARK_EPITHELIAL_MESENCHYMAL_TRANSITION	0.033	0.127	0.90	-1.28
12	HALLMARK_MYC_TARGETS_V1	0.033	0.127	0.90	1.32
13	HALLMARK_NOTCH_SIGNALING	0.032	0.127	0.90	-1.46
14	HALLMARK_TGF_BETA_SIGNALING	0.039	0.138	0.86	-1.43
15	HALLMARK_TNFA_SIGNALING_VIA_NFKB	0.043	0.144	0.84	1.3
26	**HALLMARK_OXIDATIVE_PHOSPHORYLATION**	**0.211**	**0.408**	**0.39**	**-1.08**
38	**HALLMARK_FATTY_ACID_METABOLISM**	**0.701**	**0.922**	**0.04**	**0.89**
	5 dpi	pval	padj	-log10(padj)	NES
1	HALLMARK_ADIPOGENESIS	0.00004	0.0005	3.30	-1.72
2	**HALLMARK_FATTY_ACID_METABOLISM**	**0.00004**	**0.0005**	**3.30**	**-1.89**
3	**HALLMARK_INTERFERON_GAMMA_RESPONSE**	**0.00003**	**0.0005**	**3.30**	**1.81**
4	**HALLMARK_OXIDATIVE_PHOSPHORYLATION**	**0.00004**	**0.0005**	**3.30**	**-2.17**
5	HALLMARK_ALLOGRAFT_REJECTION	0.0002	0.002	2.70	1.76
6	HALLMARK_BILE_ACID_METABOLISM	0.0004	0.003	2.52	-1.64
7	**HALLMARK_INTERFERON_ALPHA_RESPONSE**	**0.0004**	**0.003**	**2.52**	**1.77**
8	HALLMARK_PEROXISOME	0.001	0.006	2.22	-1.6
9	HALLMARK_E2F_TARGETS	0.0033	0.017	1.77	1.66
10	HALLMARK_XENOBIOTIC_METABOLISM	0.0034	0.017	1.77	-1.45
11	**HALLMARK_COMPLEMENT**	**0.0099**	**0.043**	**1.37**	**1.58**
12	**HALLMARK_INFLAMMATORY_RESPONSE**	**0.0102**	**0.043**	**1.37**	**1.57**
13	HALLMARK_G2M_CHECKPOINT	0.0129	0.049	1.31	1.53
14	**HALLMARK_MTORC1_SIGNALING**	**0.0158**	**0.053**	**1.28**	**1.5**
15	HALLMARK_TGF_BETA_SIGNALING	0.0149	0.053	1.28	-1.49
16	HALLMARK_PI3K_AKT_MTOR_SIGNALING	0.0177	0.055	1.26	1.5
17	HALLMARK_IL6_JAK_STAT3_SIGNALING	0.0303	0.089	1.05	1.46
18	HALLMARK_MITOTIC_SPINDLE	0.0416	0.104	0.98	1.37
19	HALLMARK_TNFA_SIGNALING_VIA_NFKB	0.0377	0.104	0.98	1.38
20	**HALLMARK_UNFOLDED_PROTEIN_RESPONSE**	**0.0417**	**0.104**	**0.98**	**1.4**
21	HALLMARK_GLYCOLYSIS	0.0469	0.112	0.95	-1.26
22	HALLMARK_MYOGENESIS	0.0509	0.116	0.94	-1.25
23	HALLMARK_IL2_STAT5_SIGNALING	0.0585	0.127	0.90	1.33
24	HALLMARK_ANDROGEN_RESPONSE	0.063	0.131	0.88	1.36

Table S3, related with Figure 4. Pathway enrichment analysis. Significant regulated REACTOME pathways. (FDR < 0.15 and normalized enrichment score [NES] > 0). All pathways represented in Figure 3C are highlighted in bold.

	2 dpi	pval	padj	-log10(padj)	NES
1	**REACTOME_ADAPTIVE_IMMUNE_SYSTEM**	**0.00001**	**0.0059**	2.23	**1.43**
2	**REACTOME_INNATE_IMMUNE_SYSTEM**	**0.00001**	**0.0059**	2.23	**1.47**
3	**REACTOME_CYTOKINE_SIGNALING_IN_IMMUNE_SYSTEM**	**0.00003**	**0.009**	2.05	**1.37**
4	**REACTOME_NEUTROPHIL_DEGRANULATION**	**0.00003**	**0.009**	2.05	**1.47**
5	REACTOME_IMMUNOREGULATORY_INTERACTIONS_ BETWEEN_A_LYMPHOID_AND_A_NON_LYMPHOID_CELL	0.00004	0.01	2.00	1.57
6	**REACTOME_INTERFERON_SIGNALING**	**0.00006**	**0.01**	2.00	**1.55**
7	REACTOME_CELLULAR_RESPONSES_TO_EXTERNAL_ STIMULI	0.0004	0.05	1.30	1.36
8	REACTOME_COLLAGEN_BIOSYNTHESIS_AND_MODIFYING_ENZYMES	0.0003	0.05	1.30	-1.73
9	REACTOME_DEUBIQUITINATION	0.0003	0.05	1.30	1.45
10	REACTOME_COMPLEMENT_CASCADE	0.001	0.1	1.00	1.54
11	REACTOME_SIGNALING_BY_INTERLEUKINS	0.0009	0.1	1.00	1.38
12	REACTOME_INFECTIOUS_DISEASE	0.0013	0.11	0.96	1.3
13	REACTOME_METABOLISM_OF_RNA	0.0011	0.11	0.96	1.31
14	REACTOME_SIGNALING_BY_CYTOSOLIC_FGFR1_FUSION_MUTANTS	0.0013	0.11	0.96	1.46
15	REACTOME_UB_SPECIFIC_PROCESSING_PROTEASES	0.0012	0.11	0.96	1.46
16	REACTOME_CLASS_I_MHC_MEDIATED_ANTIGEN_PROCESSING_PRESENTATION	0.0018	0.13	0.89	1.38
17	REACTOME_HIV_INFECTION	0.0021	0.14	0.85	1.44
18	REACTOME_INTERFERON_ALPHA_BETA_SIGNALING	0.0023	0.14	0.85	1.51
19	REACTOME_MISCELLANEOUS_TRANSPORT_AND_BINDING_EVENTS	0.0023	0.14	0.85	-1.6

	5 dpi	pval	padj	-log10(padj)	NES
1	REACTOME_ADAPTIVE_IMMUNE_SYSTEM	**2.17E-05**	**0.00622031**	**2.21**	**1.62**
2	**REACTOME_MITOCHONDRIAL_PROTEIN_IMPORT**	**2.67E-05**	**0.00622031**	**2.21**	**-1.77**
3	REACTOME_PROTEIN_LOCALIZATION	3.67E-05	0.00622031	2.21	-1.83
4	**REACTOME_PYRUVATE_METABOLISM_AND_CITRIC_ACID_TCA_CYCLE**	**2.56E-05**	**0.00622031**	**2.21**	**-1.82**
5	**REACTOME_RESPIRATORY_ELECTRON_TRANSPORT**	**2.91E-05**	**0.00622031**	**2.21**	**-1.91**
6	REACTOME_RESPIRATORY_ELECTRON_TRANSPORT_ATP_SYNTHESIS_BY_CHEMIOSMOTIC_COUPLING_AND_HEAT_PRODUCTION_BY_UNCOUPLING_PROTEINS_	3.14E-05	0.00622031	2.21	-1.98
7	REACTOME_THE_CITRIC_ACID_TCA_CYCLE_AND_RESPIRATORY_ELECTRON_ TRANSPORT	3.62E-05	0.00622031	2.21	-2.1
8	REACTOME_COMPLEX_I_BIOGENESIS	5.05E-05	0.00666532	2.18	-1.75
9	REACTOME_TRANSLATION	5.06E-05	0.00666532	2.18	-1.66
10	**REACTOME_METABOLISM_OF_AMINO_ACIDS_AND_DERIVATIVES**	**6.05E-05**	**0.00717182**	**2.14**	**-1.59**
11	REACTOME_IMMUNOREGULATORY_INTERACTIONS_BETWEEN_A_LYMPHOID_AND_A_NON_LYMPHOID_CELL	0.00013048	0.01405648	1.85	1.78
12	**REACTOME_INNATE_IMMUNE_SYSTEM**	**0.00022103**	**0.0201481**	**1.70**	**1.49**
13	**REACTOME_MITOCHONDRIAL_FATTY_ACID_BETA_OXIDATION**	**0.00021913**	**0.0201481**	**1.70**	**-1.69**
14	REACTOME_PEROXISOMAL_PROTEIN_IMPORT	0.00024398	0.02065076	1.69	-1.71
15	REACTOME_SIGNALING_BY_RETINOIC_ACID	0.00056378	0.04453868	1.35	-1.65
16	REACTOME_MITOCHONDRIAL_BIOGENESIS	0.00062986	0.04664865	1.33	-1.65
17	REACTOME_KERATINIZATION	0.00073634	0.05132701	1.29	-1.65
18	REACTOME_CRISTAE_FORMATION	0.00095672	0.05966877	1.22	-1.63
19	REACTOME_FORMATION_OF_THE_CORNIFIED_ENVELOPE	0.00094477	0.05966877	1.22	-1.65
20	REACTOME_GLYOXYLATE_METABOLISM_AND_GLYCINE_DEGRADATION	0.00115026	0.06815301	1.17	-1.62
21	REACTOME_CLASS_C_3_METABOTROPIC_GLUTAMATE_PHEROMONE_RECEPTORS_	0.00135993	0.07673876	1.11	1.49
22	REACTOME_MOLECULES_ASSOCIATED_WITH_ELASTIC_FIBRES	0.00167998	0.09048965	1.04	-1.61
23	REACTOME_CITRIC_ACID_CYCLE_TCA_CYCLE_	0.00191307	0.09445767	1.02	-1.57
24	REACTOME_PYRUVATE_METABOLISM	0.00187531	0.09445767	1.02	-1.59
25	**REACTOME_CYTOKINE_SIGNALING_IN_IMMUNE_SYSTEM**	**0.00243127**	**0.115242**	**0.94**	**1.44**
26	REACTOME_PHASE_II_CONJUGATION_OF_COMPOUNDS	0.00304632	0.13526861	0.87	-1.56
27	REACTOME_STING_MEDIATED_INDUCTION_OF_HOST_IMMUNE_RESPONSES	0.00308207	0.13526861	0.87	1.49

Table S3, related with Figure 4. Pathway enrichment analysis. Significant regulated KEGG pathways. (FDR < 0.15 and normalized enrichment score [NES] > 0). All pathways represented in Figure 3C are highlighted in bold.

	2 dpi	pval	padj	-log10(padj)	NES
1	KEGG_SYSTEMIC_LUPUS_ERYTHEMATOSUS	0.0004	0.07	1.15	1.55
2	KEGG_COMPLEMENT_AND_COAGULATION_CASCADES	0.0015	0.14	0.85	1.53

	5 dpi	pval	padj	-log10(padj)	NES
1	KEGG_ALZHEIMERS_DISEASE	0.000036	0.002	2.70	-1.92
2	KEGG_HUNTINGTONS_DISEASE	0.000038	0.002	2.70	-1.94
3	KEGG_OXIDATIVE_PHOSPHORYLATION	0.000031	0.002	2.70	-1.96
4	KEGG_PARKINSONS_DISEASE	0.000031	0.002	2.70	-1.82
5	KEGG_VALINE_LEUCINE_AND_ISOLEUCINE_DEGRADATION	0.000074	0.003	2.52	-1.73
6	KEGG_CITRATE_CYCLE_TCA_CYCLE	0.0001	0.004	2.40	-1.68
7	KEGG_FATTY_ACID_METABOLISM	0.0002	0.005	2.30	-1.69
8	KEGG_BUTANOATE_METABOLISM	0.0003	0.007	2.15	-1.65
9	**KEGG_CARDIAC_MUSCLE_CONTRACTION**	**0.0009**	**0.015**	**1.82**	**-1.64**
10	KEGG_PEROXISOME	0.0008	0.015	1.82	-1.64
11	KEGG_PROPANOATE_METABOLISM	0.0007	0.015	1.82	-1.63
12	KEGG_GLYCOLYSIS_GLUCONEOGENESIS	0.0018	0.027	1.57	-1.62
13	KEGG_PYRUVATE_METABOLISM	0.0025	0.036	1.44	-1.6
14	KEGG_SULFUR_METABOLISM	0.0039	0.052	1.28	-1.49
15	KEGG_ALLOGRAFT_REJECTION	0.0082	0.073	1.14	1.53
16	KEGG_AMINOACYL_TRNA_BIOSYNTHESIS	0.0073	0.073	1.14	-1.55
17	KEGG_AUTOIMMUNE_THYROID_DISEASE	0.0079	0.073	1.14	1.54
18	KEGG_CELL_ADHESION_MOLECULES_CAMS	0.0083	0.073	1.14	1.61
19	KEGG_CYTOSOLIC_DNA_SENSING_PATHWAY	0.0068	0.073	1.14	1.58
20	KEGG_NATURAL_KILLER_CELL_MEDIATED_CYTOTOXICITY	0.0072	0.073	1.14	1.63
21	KEGG_NEUROACTIVE_LIGAND_RECEPTOR_INTERACTION	0.0082	0.073	1.14	1.6
22	KEGG_GRAFT_VERSUS_HOST_DISEASE	0.0101	0.081	1.09	1.53
23	KEGG_T_CELL_RECEPTOR_SIGNALING_PATHWAY	0.01	0.081	1.09	1.58
24	**KEGG_ARRHYTHMOGENIC_RIGHT_VENTRICULAR_CARDIOMYOPATHY_ARVC**	**0.0134**	**0.083**	**1.08**	**-1.47**
25	KEGG_B_CELL_RECEPTOR_SIGNALING_PATHWAY	0.0121	0.083	1.08	1.55
26	KEGG_CHEMOKINE_SIGNALING_PATHWAY	0.0135	0.083	1.08	1.54
27	KEGG_PPAR_SIGNALING_PATHWAY	0.0109	0.083	1.08	-1.49
28	KEGG_RIBOSOME	0.0132	0.083	1.08	-1.46
29	KEGG_SYSTEMIC_LUPUS_ERYTHEMATOSUS	0.012	0.083	1.08	1.55
30	**KEGG_VIRAL_MYOCARDITIS**	**0.0133**	**0.083**	**1.08**	**1.54**
31	KEGG_FC_GAMMA_R_MEDIATED_PHAGOCYTOSIS	0.0143	0.085	1.07	1.53
32	KEGG_VALINE_LEUCINE_AND_ISOLEUCINE_BIOSYNTHESIS	0.0158	0.091	1.04	-1.42
33	KEGG_BETA_ALANINE_METABOLISM	0.0182	0.102	0.99	-1.48
34	KEGG_BASAL_CELL_CARCINOMA	0.0199	0.105	0.98	-1.46
35	KEGG_RNA_POLYMERASE	0.02	0.105	0.98	-1.48
36	KEGG_LYSINE_DEGRADATION	0.0246	0.126	0.90	-1.46
37	KEGG_TOLL_LIKE_RECEPTOR_SIGNALING_PATHWAY	0.026	0.129	0.89	1.47
38	KEGG_PRIMARY_IMMUNODEFICIENCY	0.028	0.132	0.88	1.46
39	KEGG_RIG_I_LIKE_RECEPTOR_SIGNALING_PATHWAY	0.0279	0.132	0.88	1.47
40	KEGG_JAK_STAT_SIGNALING_PATHWAY	0.0292	0.134	0.87	1.44
41	KEGG_CELL_CYCLE	0.0308	0.137	0.86	1.43
42	KEGG_TRYPTOPHAN_METABOLISM	0.0312	0.137	0.86	-1.44
43	KEGG_CALCIUM_SIGNALING_PATHWAY	0.0324	0.139	0.86	-1.31

Table S5. Histopathological assessment of H&E sections for *Mavs*$^{-/-}$ infected mice (Related to Figure 7)

Mouse ID	Genotype	Dpi (days)	Condition	Vasculitis			Other Findings
				Vasculitis	Ao	PA	
M1	*Mavs*$^{-/-}$	Mock-infected	DMEM	NO	no	no	
M2	*Mavs*$^{-/-}$	Mock-infected	DMEM	NO	no	no	
M3	*Mavs*$^{-/-}$	Mock-infected	DMEM	NO	no	no	
M4	*Mavs*$^{-/-}$	Mock-infected	DMEM	NO	no	no	
M5	*Mavs*$^{-/-}$	10 dpi	CHIKV	YES	na*	yes	Focal inflammation in RA endocardium
M6	*Mavs*$^{-/-}$	10 dpi	CHIKV	YES	no	yes	
M7	*Mavs*$^{-/-}$	10 dpi	CHIKV	YES	yes	yes	
M8	*Mavs*$^{-/-}$	15 dpi	CHIKV	YES	yes	yes	
M9	*Mavs*$^{-/-}$	15 dpi	CHIKV	YES	na*	yes	
M10	*Mavs*$^{-/-}$	15 dpi	CHIKV	YES	yes	yes	Focal myocarditis in LV
M11	*Mavs*$^{-/-}$	15 dpi	CHIKV	YES	yes	yes	Multifocal myocarditis **(Figure 7A)**
M12	*Mavs*$^{-/-}$	15 dpi	CHIKV	YES	yes	yes	Multifocal myocarditis Vasculitis of intramyocardial arteries
M13	*Mavs*$^{-/-}$	15 dpi	CHIKV	YES	yes	yes	Multifocal myocarditis accentuated around the vessels
M14	*Mavs*$^{-/-}$	30 dpi	CHIKV	YES	yes	yes	
M15	*Mavs*$^{-/-}$	30 dpi	CHIKV	NA*	na*	na*	
M16	*Mavs*$^{-/-}$	30 dpi	CHIKV	YES	yes	yes	Focal myocarditis in LV
M17	*Mavs*$^{-/-}$	30 dpi	CHIKV	YES	yes	yes	Multifocal myocarditis accentuated around the vessels **(Figure 7A)**
M18	*Mavs*$^{-/-}$	30 dpi	CHIKV	YES	yes	yes	

na*: no Ao or PA section in that slide; Ao: aorta; PA: pulmonary artery; RA: Right atrium; LV: Left ventricle